Metals & corrosion

Unveiling the macrosegregation formation mechanism and its impact on properties in dissimilar welding between CoCrFeMnNi high-entropy alloy and 316 stainless steel

Jiajia Shen[1,2,*] , Rae Eon Kim[3], Martim Mestre[1,2], J. G. Lopes[1], Jingjing He[4], Jin Yang[5], Zhi Zeng[6], N. Schell[7], Hyoung Seop Kim[3,8,9], and J. P. Oliveira[1,2]

[1] UNIDEMI, Department of Mechanical and Industrial Engineering, NOVA School of Science and Technology, Universidade NOVA de Lisboa, 2829-516 Caparica, Portugal

[2] CENIMAT/I3N, Department of Materials Science, NOVA School of Science and Technology, Universidade NOVA de Lisboa, 2829-516 Caparica, Portugal

[3] Graduate Institute of Ferrous Technology, POSTECH (Pohang University of Science and Technology), Pohang 37673, South Korea

[4] Advanced Manufacturing Center, Ningbo Institute of Technology, Beihang University, Ningbo 315800, China

[5] School of Materials Engineering, Shanghai University of Engineering Science, Shanghai 201620, China

[6] School of Mechanical and Electrical Engineering, University of Electronic Science and Technology of China, Sichuan 611731, China

[7] Institute of Materials Physics, Helmholtz-Zentrum Hereon, Max-Planck-Str. 1, 21502 Geesthacht, Germany

[8] Department of Materials Science and Engineering, POSTECH (Pohang University of Science and Technology), Pohang 37673, South Korea

[9] Institute for Convergence Research and Education in Advanced Technology, Yonsei University, Seoul 03722, South Korea

ABSTRACT

High-entropy alloys (HEAs) are increasingly preferred as structural materials in nuclear engineering and aerospace applications. These fields often require the design of dissimilar joints. Here, gas tungsten arc welding (GTAW) was used for the first time to join CoCrFeMnNi HEAs with 316 stainless steel. Microstructural characterization, including electron microscopy, high-energy synchrotron X-ray diffraction, and thermodynamic calculations, along with micro- and macroscale mechanical assessments, was utilized. These methods were instrumental in evaluating and clarifying the effects of the non-equilibrium solidification and weld thermal cycle on the microstructure evolution of the joint. In the fusion zone (FZ), distinctive peninsula-shaped macroscopic segregation area is observed, with its formation being related to the liquidus temperature differences between the base materials (BMs) and the welded metal, compounded by the Marangoni effect. The weld thermal cycle was found to promote multiple solid-state phase

transformations in the heat-affected zone (HAZ) adjacent to the CoCrFeMnNi BM, leading to varying degrees of softening. The HAZ near the 316 stainless steel BM maintained its original microstructural and mechanical properties. Fracture predominantly occurred in the FZ, mainly due to the interplay of large columnar grains, macrosegregation effects, and emergence of BCC and σ brittle phases due to the complex chemistry within this region. Thermodynamic modeling validated the formation of these phases. The ultimate tensile strength and elongation at room temperature were approximately ≈493 MPa and ≈10.70%, respectively.

Introduction

High-entropy alloys, particularly the equiatomic CoCrFeMnNi HEA [1, 2], have attracted considerable attention in the field of high-performance material design due to their exceptional mechanical properties, such as excellent tensile ductility, fracture toughness, and impressive low-temperature performance. Such superior mechanical performance of the CoCrFeMnNi HEA has foreseen potential applications in various field such as in liquefied gas storage, various engines, and nuclear applications [3]. Recent research endeavors have predominantly focused on the phase formation, composition, mechanical properties, and evaluation of physical and chemical properties [4, 5]. However, before contemplating industrial applications, the weldability of these materials is a critical concern since the deployment of any engineering structural component heavily depends on the successful use of welding technologies.

Presently, laser welding is gaining prominence due to its high efficiency and a narrow extension of both fusion zone (FZ) and heat-affected zone (HAZ). Nevertheless, its widespread industrial adoption may be hindered by elevated initial costs. Conversely, GTAW's technical maturity allows for easy technology transfer, as many technicians are experienced in its operation. Additionally, its cost-effectiveness makes it well suited for large-scale production and cost-sensitive projects. With meticulous adjustment of process parameters, GTAW can yield fully penetrated, defect-free, and high-performance welded joints. Therefore, evaluating the processability or weldability of new materials, particularly dissimilar joints such as CoCrFeMnNi/316 stainless steel, is crucial for their successful application in engineering structures. The weldability of CoCrFeMnNi/316 stainless steel dissimilar joints is assessed by examining the microstructural evolution, mechanical properties, and macrosegregation behavior

during gas tungsten arc welding (GTAW). The distinct characteristics of these joints, including the formation of peninsula-shaped segregation areas in the fusion zone and the impact of welding parameters on mechanical performance, highlight the unique challenges of welding high-entropy alloys (HEAs) with conventional stainless steels. Moreover, during welding, the thermal cycle can drastically modify the original microstructure of the base material (BM), as well as that in the HAZ and FZ. Rapid melting and non-equilibrium solidification can foster the formation of non-equilibrium phases which, depending on the phases formed, can diminish the mechanical performance and potentially cause for premature joint failure. This is particularly significant in dissimilar welding, where commonly segregation, resulting from uneven solute distribution, can substantially compromise the joint's strength, toughness, and corrosion resistance [6–9]. These potential hazards can be mitigated by timely adjustments to alloy composition and microstructure. Therefore, evaluating the relationship between microstructure, mechanical properties, and processability is needed before integrating these new materials into engineering structural applications. Here, it is important to note that the thermal cycle is an inherent phenomenon in welding. Although this study does not provide quantitative descriptions, its existence is indirectly verified through the experimental design and results. During welding, the localized heat source (the arc) rapidly heats the material to a molten state (FZ), followed by rapid cooling as the heat source moves or the process concludes. This constitutes a single cycle of the weld thermal process. The application of weld thermal cycles is achieved by controlling welding parameters such as welding current, voltage, and welding speed. These parameters determine the magnitude and distribution of heat input, significantly impacting microstructural evolution (e.g., solid-state phase transformations) and mechanical

properties. The specific effects of weld thermal cycles on microstructure and mechanical properties are detailed discussed in the following section.

So far, research on welding of CoCrFeMnNi HEAs remains insufficient, with a notable gap in studies specifically addressing dissimilar welding between CoCrFeMnNi HEAs and traditional alloys. Existing literature underscores the favorable weldability of the CoCrFeMnNi HEA in similar welding scenarios [10–17], encompassing various welding processes such electron beam welding, laser welding, and solid-state routes. However, considering the high costs associated to HEAs, their applications are often confined to critical structural components. Consequently, there is a comprehensive research on dissimilar welding between CoCrFeMnNi HEA and traditional structural alloys. The research enables economically efficient manufacturing of structures, as well as providing valuable information in instance where dissimilar welding between different alloys is required to streamline design and reduce costs. Dissimilar welding offers increased design flexibility for deployment under diverse conditions. Although some studies have explored dissimilar welding between the CoCrFeMnNi HEA and traditional alloys, such investigations are relatively scarce, with only 15 reported cases [18–32]. Among these studies, only one case utilized GTAW to examine the weldability of CoCrFeMnNi to 304 stainless steel. Therefore, future research must expand further, exploring the possibility of using welding technologies to dissimilarly weld the CoCrFeMnNi HEA to traditional, highly used metals. These efforts will broaden the application scope of different types of alloys and reveal their potential in the field of engineering.

This study focuses on the weldability of as-rolled CoCrFeMnNi HEA and annealed 316 stainless steel using GTAW. The research into dissimilar joining of CoCrFeMnNi HEAs and 316 stainless steel is motivated by the goal of optimizing multimaterial performance. CoCrFeMnNi HEAs, as a new class of multi-principal-element alloys, offer exceptional high-temperature mechanical properties, wear resistance, and radiation resistance. In contrast, 316 stainless steel is well known for its superior corrosion resistance, mechanical properties, and good machinability. The objective of combining these two materials through dissimilar joining technologies is to achieve complementary performance characteristics suitable for extreme operating conditions. For example, in

nuclear reactors, materials must endure extreme temperatures, high pressures, and intense radiation. The integration of CoCrFeMnNi HEAs' high-temperature and radiation-resistant properties with 316 stainless steel's corrosion resistance can greatly enhance the performance of nuclear engineering components, such as fuel cladding and heat exchangers, extending their service life and reducing maintenance costs. In aerospace applications, components like turbine blades and combustion chambers are exposed to high temperatures, high pressures, and complex stress conditions. The design of dissimilar joints between CoCrFeMnNi HEA and 316 stainless steel aims to balance high strength, toughness, and corrosion resistance, while significantly enhancing the overall performance and fuel efficiency of aircraft by reducing weight. However, despite the many advantages of dissimilar joining between CoCrFeMnNi HEAs and 316 stainless steel, several challenges persist for process implementation. These include potential issues related to the differences in thermal expansion coefficients between the materials and metallurgical compatibility.

Therefore, in the current work, in-depth insights into the structural characteristics of the welded joints were obtained through advanced characterization techniques including electron microscopy and synchrotron X-ray diffraction analysis. These techniques were employed to investigate the impact of the weld thermal cycle on the microstructure across the welded joints, further aided by thermodynamic calculations. Additionally, microhardness mapping and tensile testing were conducted to assess the mechanical properties of the welded joints. The primary objective of this research is to unveil the correlations between processing, structure, and resulting mechanical properties, further leveraged by thermodynamic modeling. This study aims to provide theoretical guidance and practical foundations for future dissimilar welding endeavors involving HEAs and traditional engineering alloys.

Experimental procedure

Materials

In this study, dissimilar welding was conducted using self-prepared CoCrFeMnNi HEA and commercially obtained 316 stainless as the BMs. The CoCrFeMnNi HEA was prepared by initially obtaining an ingot through vacuum induction melting. Subsequently,

cold rolling was carried out at room temperature, reducing the material thickness from 3 to 1.5 mm. Meanwhile, commercially available 316 stainless steel with a thickness of 1.5mm was purchased from MLGInox. It underwent hot rolling from 10 to 3mm thickness at 1050°C, followed by cold rolling to the final material thickness. The stainless steel was further annealed at 1050°C for 1 min and subsequently water-quenched.

Prior to welding, both the CoCrFeMnNi HEA and 316 stainless steel sheets were precision-cut into thin plates with dimensions of 40 × 40 × 1.5mm. Subsequently, the surfaces and cut edges of the samples were wiped with ethanol and acetone to remove any residues from the cutting process and eliminate potential contaminants. These steps were implemented to ensure the high quality of the welding process and the reliability of the welded joints.

Gas metal arc welding

To investigate the weldability between the as-rolled CoCrFeMnNi and the 316 stainless steel, GTAW was employed. A schematic diagram is illustrated in Fig. 1a. A TELWIN Technology TIG 182 AC/DC-HF/LIFT welding machine, equipped with a 1.6 mm, 2% lanthanated tungsten electrode, was utilized with direct current (DC). The selection of welding parameters aimed at achieving a fully penetrated joint with minimal heat input. After preliminary testing, optimal parameters were determined as follows: current 65 A, voltage 12.6 V, speed 2 mm/s, and heat input of 409.5 J/mm. To prevent oxidation and contamination from the surrounding atmosphere during welding, 99.99% pure Ar was employed as the inert shielding gas on the top and bottom surfaces of the workpiece, with a flow rate of 16 L/min. Additionally, the protective gas was opened 2 s before the start of welding and closed 6 s after its completion to minimize oxidation. Then, the welded joints were cut into dog-bone-shaped specimens using an electrical discharge cutting machine for further structural and mechanical characterization.

Microstructure and mechanical characterization

To comprehensively characterize the microstructure of the welded joint, the following procedure was performed. The initial step involves embedding the metallographic samples in epoxy resin. Subsequently, mechanical grinding is performed using SiC sandpapers, progressing from 320 to 4000 grit sequentially to achieve proper surface condition. Following grinding, the sample undergoes a polishing procedure utilizing 3 μm diamond paste until a mirror-like finish is attained on the sample surface. Eventually, to reveal the microstructure, the polished specimen is immersed in a Kalling's No. 2 etching solution, to reveal the different microstructural constituents. For microstructure analysis, a Leica DMI 5000 M inverted optical microscope was employed to observe the microstructure of different regions of the welded joint. For quantitative studies of grain morphology, crystal structure, and elemental distributions, a combination of electron backscatter diffraction (EBSD) and energy-dispersive spectroscopy (EDS) measurements were performed. EBSD measurements were performed using a field-emission scanning electron microscopy (FE-SEM;
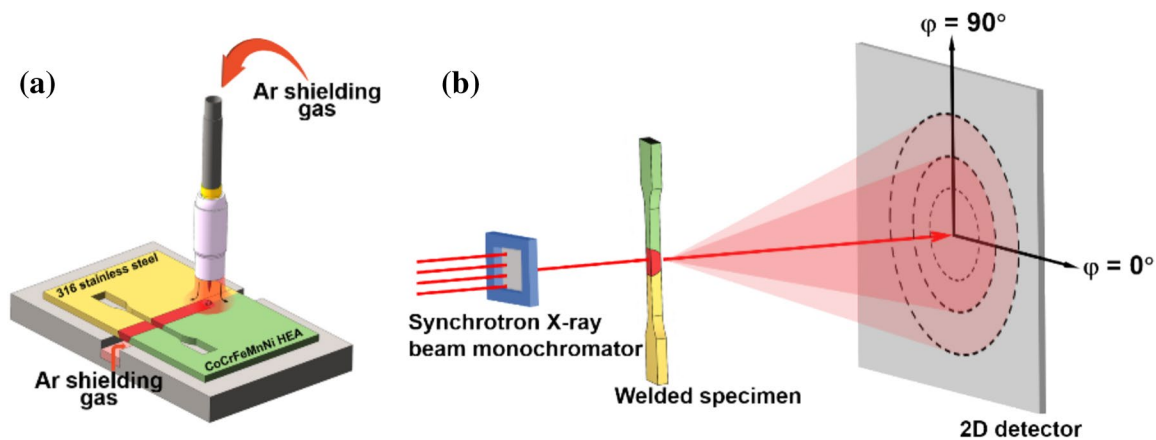

Figure 1 **a**: Schematic of the gas tungsten arc welding setup used in this work; **b**: synchrotron X-ray diffraction setup (not to scale).

Philips, FEG-XL30S). TSL OIM Analysis 7.2 software was used for post-processing the EBSD raw data. SEM/EDS measurements were performed using a FE-SEM (JEOL, JEM-2100F).

To further investigate the impact of the weld thermal cycle on the microstructural evolution of the dissimilar joints, high-energy synchrotron X-ray diffraction (SXRD) experiments were conducted in the High Energy Materials Science (HEMS) P07 beamline at PETRA III/DESY. A wavelength of 0.14235 Å, corresponding to a high-energy beam of 87 keV, was utilized. The incident beam spot size was set at 200 × 200 µm, with the scanning direction perpendicular to the weld line. The scanned regions started on the CoCrFeMnNi BM, passing through the HAZ and FZ, extending all the way to the opposite stainless steel BM. The

total length of the scan was approximately ≈6 mm, with 200 µm between adjacent analyzed points. A Perkin-Elmer 2D detector was employed to capture the 2D Debye–Scherrer diffraction ring images, positioned at a distance of approximately ≈1.36 m from the sample, as determined using LaB$_6$ calibrant powder. The schematic representation of the setup used is shown in Fig. 2b. The diffraction material analysis using diffraction (MAUD) program was utilized for post-processing the raw data obtained from synchrotron radiation.

ThermoCalc is a specialized tool for conducting thermodynamic calculations, featuring the Scheil-Gulliver module specifically designed for predicting the solidification process evolution under non-equilibrium conditions. In this study, the TCHEA5.2 HEA database
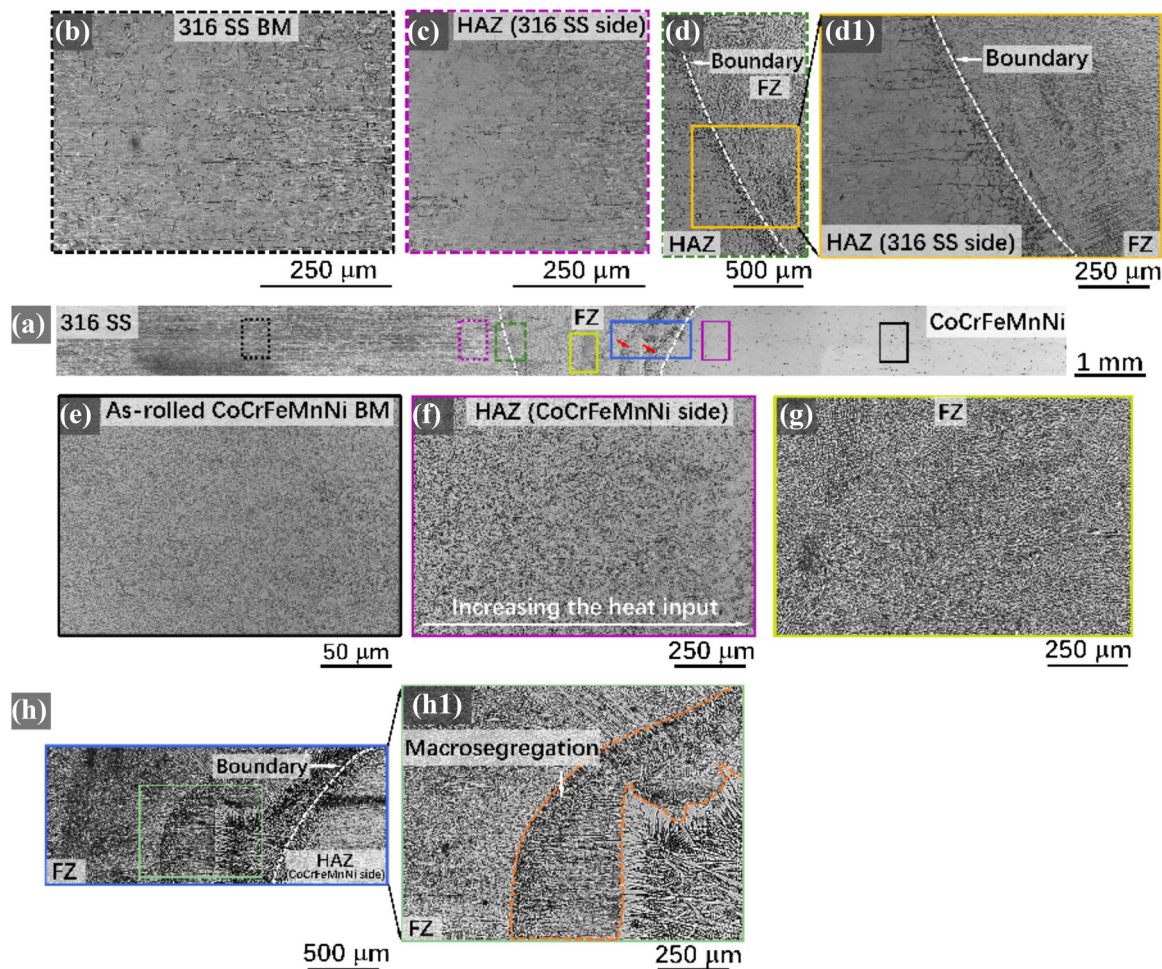

Figure 2 Light optical microscopy of the gas tungsten arc welded CoCrFeMnNi and 316 stainless steel dissimilar welded joint. **a**: overview of the cross section of the welded joint; **b**), c), **d**), e), **f**), h) and **g**): represent the BM, HAZ and HAZ/FZ boundary on the 316 stainless steel side, and the BM, HAZ and HAZ/FZ boundary on the CoCrFeMnNi side, respectively; d1) and h1): detail close-up views of HAZ/FZ boundary on the stainless steel and HEA sides, respectively.

was utilized for the employed thermodynamic calculations, aiming to predict the solidification path, and resulting solidification phase structures in the FZ during non-equilibrium solidification. It helps to understand the mechanisms underlying the formation of the FZ, especially during dissimilar joining owing to the complex mixture that develops. Through a comparison between the thermodynamically predicted phase structures with experimentally observed ones, the precision and applicability of the HEA thermodynamic database and the Scheil-Gulliver model can be validated and improved, if needed.

To establish correlations between welding process conditions, microstructure evolution, and mechanical properties, micro- to macroscale mechanical characterization was also conducted. Microhardness measurements were performed using a Mitutoyo-HM-112 hardness testing machine along the transverse section of the weld joint. The measurements started on one of the BMs, moved through the HAZ and FZ, and reached the opposite BM. To explore how the weld thermal cycles affect the microhardness behavior over the welded joint, hardness tests were conducted at different heights along the cross section of the sample. A load of 500 g was applied for a duration of 10 s, with a step size of 200 μm between consecutive indentations in both transverse and longitudinal directions. Uniaxial tensile tests at room temperature were carried out to evaluate the mechanical response on a Shimazu testing machine, equipped with a 50 kN load cell, employing a tensile strain rate of 1×10^{-3}s. The loading direction was perpendicular to the welding direction. To ensure the reproducibility of the mechanical properties of the welded joint, three specimens underwent tensile testing under the same tensile testing conditions. The fracture surfaces of the welded specimen's post-tensile failure were examined using a Hitachi SU3800 scanning electron microscope (SEM).

Results and discussions

Microstructure evolution

The macroscopic observation of the microstructure of the dissimilar welded joint between CoCrFeMnNi and 316 stainless is presented in Fig. 2. As evident from Fig. 2, the welded joint showcases excellent weld geometry, complete penetration, and no visible defects such as pores and cracks on the cross-sectional view.

In Fig. 2a, the HAZ/FZ boundaries are highlighted by white dashed lines.

Optical micrographs are first used to understand the macroscale structure evolution across the joint. First and foremost, attention is directed toward the two base materials: CoCrFeMnNi HEA and 316 stainless steel, as shown in Fig. 2b and e, respectively. The CoCrFeMnNi BM, having undergone cold rolling prior to welding, exhibits a refined grain structure (refer to Fig. 2e) of approximately ≈0.27μm, which is significantly smaller compared to the grain sizes in the HAZ (≈14.18 μm) and the FZ (≈91.53 μm) (Fig. 6b). In contrast, the stainless steel BM, subjected to annealing before welding, displays a distinct equiaxed grain morphology. As moving into the HAZ near the stainless steel (refer to Fig. 2c), the crystal structure maintains an equiaxed grain morphology. However, approaching the FZ near this HAZ a typical dendritic solidification structure appears (refer to Fig. 2d1). These structures nucleate on the cold BM along the HAZ/FZ boundary and exhibit typical dendritic growth. Similarly, upon entering the HAZ near the CoCrFeMnNi side, microstructural changes induced by the weld thermal cycle become evident. The original pancake-shaped and highly deformed grains (see Fig. 2e) transform into equiaxed grains (refer to Fig. 2f), representing typical characteristics of a recrystallized microstructure. Approaching the FZ boundary, a noticeable coarsening of the grain structure occurs. Therefore, two primary driving forces govern the solid-state phase transformations (recovery, recrystallization and grain growth) in the HAZ near the CoCrFeMnNi side: One is the high plastic strain energy pre-stored in the BM, and the other one is the weld thermal cycle. In fact, the combined effect of the previously imposed deformation (due to cold rolling), compounded by a gradient of the experienced peak temperature from the BM to the FZ boundary will promote recovery at the beginning of the HAZ, grain coarsening close to the FZ, while in between recrystallization is predominant.

Advancing into the FZ from the CoCrFeMnNi HAZ side, distinct dendritic solidification structures are observed (refer to Fig. 2h). However, near the central region of the FZ, the solidification structure transitions from dendritic near the HAZ/FZ boundary to a mixture of equiaxed and cellular grains (refer to Fig. 2g). The microstructural morphology during this solidification process is primarily determined by the ratio of undercooling or temperature gradient (G)

to the growth rate (R) [33]. This ratio can be used to assess the majority of the solidification microstructures that are formed in the weld metal. Specifically, near the HAZ/FZ boundary, higher G and smaller R exist, which combined with a lower undercooling rate predominantly results in dendritic growth. However, in the central region of the weld, typically characterized by lower G values and larger R values, a higher undercooling rate is observed. Thus, from the HAZ/FZ boundary to the central region of the FZ, the solidification structure exhibits a transition from dendritic growth to competitive elimination and free nucleation, resulting in the formation of cellular and equiaxed grains. An interesting observation is the distinct microstructural differences observed in the HAZ near the 316 stainless steel and CoCrFeMnNi sides. On the 316 stainless steel side, the HAZ features large columnar grains with highly concentrated orientations, whereas on the CoCrFeMnNi side, the HAZ exhibits fine equiaxed grains without significant preferential orientation. The fundamental reason for these differences lies in the variations between the two BMs (316 stainless steel and CoCrFeMnNi HEA) in terms of their solidus–liquidus temperature range and cooling rates, which directly influence the G/R ratio. Additionally, fluid flow within the molten pool and differences in solute distribution serve as auxiliary factors, further impacting the grain morphology in the respective regions.

A noteworthy phenomenon is the occurrence of macroscopic segregation in these dissimilar joints, as indicated by the red arrows in Fig. 2a. This phenomenon is highlighted in the high-magnification image, presented in Fig. 2h1. Indeed, macroscopic segregation is a common phenomenon in dissimilar welded joints, primarily arising from compositional variations between the bulk welded zone and the BMs, coupled with subsequent differences in liquidus and solidification temperature range between BMs and different regions within the FZ due to the Marangoni effect [34, 35]. These differences result in solute segregation at a macroscopic scale throughout the welded joint, often described as peninsulas, beaches, and/or islands, depending on their morphology. If the liquidus temperature of the weld pool (T_{L-FZ}) is lower than that of one of the BMs (T_{L-BM}), i.e., $T_{L-FZ} < T_{L-BM}$, peninsulas or islands with chemical compositions similar to one of the BMs may form. Conversely, if the liquidus temperature of the weld pool is higher than the temperature of the BMs ($T_{L-FZ} > T_{L-BM}$), irregularly shaped

beaches with compositions similar to one of the BMs may develop [34]. Apart from compositional changes, in the vicinity of the HAZ/FZ boundary and even far from the HAZ/FZ boundary, the microstructure and composition are often distinctly different from the surrounding bulk weld metal. These features are compositionally closer to, and often identical with, the nearby BM. For the CoCrFeMnNi/stainless steel dissimilar joint, the mechanisms underlying the formation of the observed macroscopic segregation will be further investigated throughout this work, combining EDS analysis and thermodynamic simulations, to comprehensively understand the causes and evolution of macroscopic segregation. Here, in comparing the prior study [36] with this work, we observed that while peninsula-shaped macrosegregations were not detected in the two-dimensional cross-sectional microstructures of as-annealed CoCrFeMnNi and annealed 316 stainless steel joints, this does not rule out their presence. Welded joints are three-dimensional structures, and the dynamic interactions of convection, thermal gradients, and solidification processes within the molten pool led to highly non-uniform and localized microstructures. As these macrosegregations are distributed unevenly, their detection depends heavily on the selected cross-sectional location. Hence, the absence of such features in one study does not imply their complete absence from the joint. Furthermore, it should be noted that quantifying the exact frequency of these macrosegregations across the entire joint is challenging. Their occurrence frequency depends on factors such as the fluid dynamics within the weld pool and thermal input. Since the welded joint is a three-dimensional structure as we mentioned before, the actual distribution of peninsula-shaped macrosegregation forms in the three-dimensional weld pool, while what we observe is the manifestation in two-dimensional cross sections. Therefore, although segregated regions may frequently appear in some cross sections, such segregation may vary due to changes in the analyzed cross section and differences in local solidification dynamics.

To further assess the macrosegregation phenomenon observed in the FZ, high-resolution EDS analysis of the elemental distribution in the entire dissimilar welding joint is depicted in Fig. 3. The blue dashed line represents the boundary between the HAZ and FZ, and its determination relies on the microstructural morphology of the FZ illustrated in Fig. 3a. Examining the elemental distribution map (refer to Fig. 3b), it is
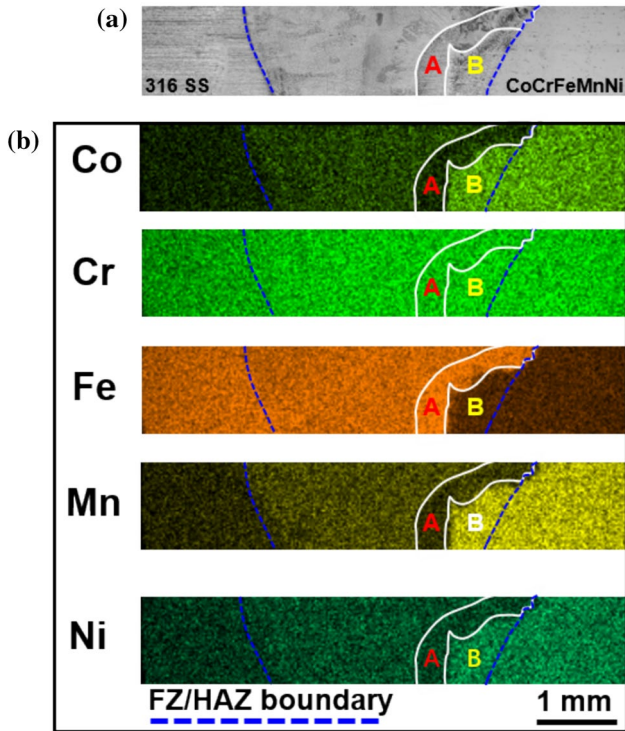
Figure 3 **a**: Optical micrograph of the CoCrFeMnNi and 316 stainless steel dissimilar welded joint; **b** EDS mapping of the dissimilar welded joint corresponding to Fig. 3 **a**.

straightforward to distinguish the HAZ/FZ boundary on the left side of the FZ, and its position aligns with the observations from the joint morphology. However, the HAZ/FZ boundary adjacent to the CoCrFeMnNi side, as discerned through EDS compositional analysis, is anticipated to coincide with the white line delineated between the letters A and B (refer to Fig. 3b), which is, however, different from the position of the HAZ/FZ boundary line, as determined by the morphology features illustrated in Fig. 2a. This diverges from the position of the HAZ/FZ boundary determined through microstructural morphology observation. The primary reason for this apparent inconsistency is related to the macrosegregation commonly found in dissimilar welded joints, resulting in the elemental distribution in region B (refer to Fig. 3b) closely resembling the chemical composition of the CoCrFeMnNi BM. Consequently, accurately distinguishing the HAZ/FZ boundary on the right side of the FZ based solely on EDS compositional changes is challenging. In such cases, combining changes in the microstructural features of the FZ provides a more accurate depiction of the HAZ/FZ boundary. The

mechanism behind this macrosegregation is not only due to differences in the chemical composition of the BMs used in dissimilar joints but is more significantly influenced by the temperature difference between the liquidus lines of the bulk weld metal in FZ and the BMs. Apart from region B, region A represents another distinctive segregation region, taking the shape of a regular peninsula. The occurrence of region A is similarly attributed to the temperature difference between the liquidus lines of the BM and the bulk weld metal region. Further detailed discussions on how the liquidus temperatures affect macrosegregation in the FZ of dissimilar joints will be presented when presenting Fig. 4.

In addition to the abovementioned factors (differences in BM composition and liquidus temperatures differences), the non-equilibrium solidification during welding involves complex transport phenomena, including heat transfer, localized chemical composition variations, and fluid flow, which makes the analysis more complex. This complexity exacerbates the influence of the Marangoni flow on the chemical composition of the FZ, serving as an additional factor contributing to the existence of macrosegregation. Examining the macrosegregation domain of region A reveals an enrichment in Fe, and a depletion in Co, Ni, and Mn. The EDS brightness levels of these elements in region A, as observed in the EDS mapping, closely resemble that of the 316 stainless steel BM. As for region B, the enrichment levels of all elements (Fe, Mn, Co, Cr, and Ni) align well with the CoCrFeMnNi BM, although the content of Fe is significantly reduced compared to region A and the bulk weld metal in the FZ. Through compositional distribution analysis of regions, A and B, it can be predicted that this region originates from unmixed 316 stainless steel and CoCrFeMnNi BM, respectively.

For a comprehensive evaluation of the microstructural evolution within the CoCrFeMnNi-316SS dissimilar welded joint, large-scale EBSD mapping was employed (refer to Fig. 4a). EBSD data for the as-rolled CoCrFeMnNi BM are not included as this material condition state has been extensively reported in previous studies [37]. In Fig. 4a, the boundaries of the HAZ and FZ are delineated by blue solid lines. By combining this information with the macroscopic overview of the welded joint in Fig. 2a, it becomes evident that there are no macroscopic defects (such as visible pores, inclusions and cracks). This observation suggests a good metallurgical compatibility between
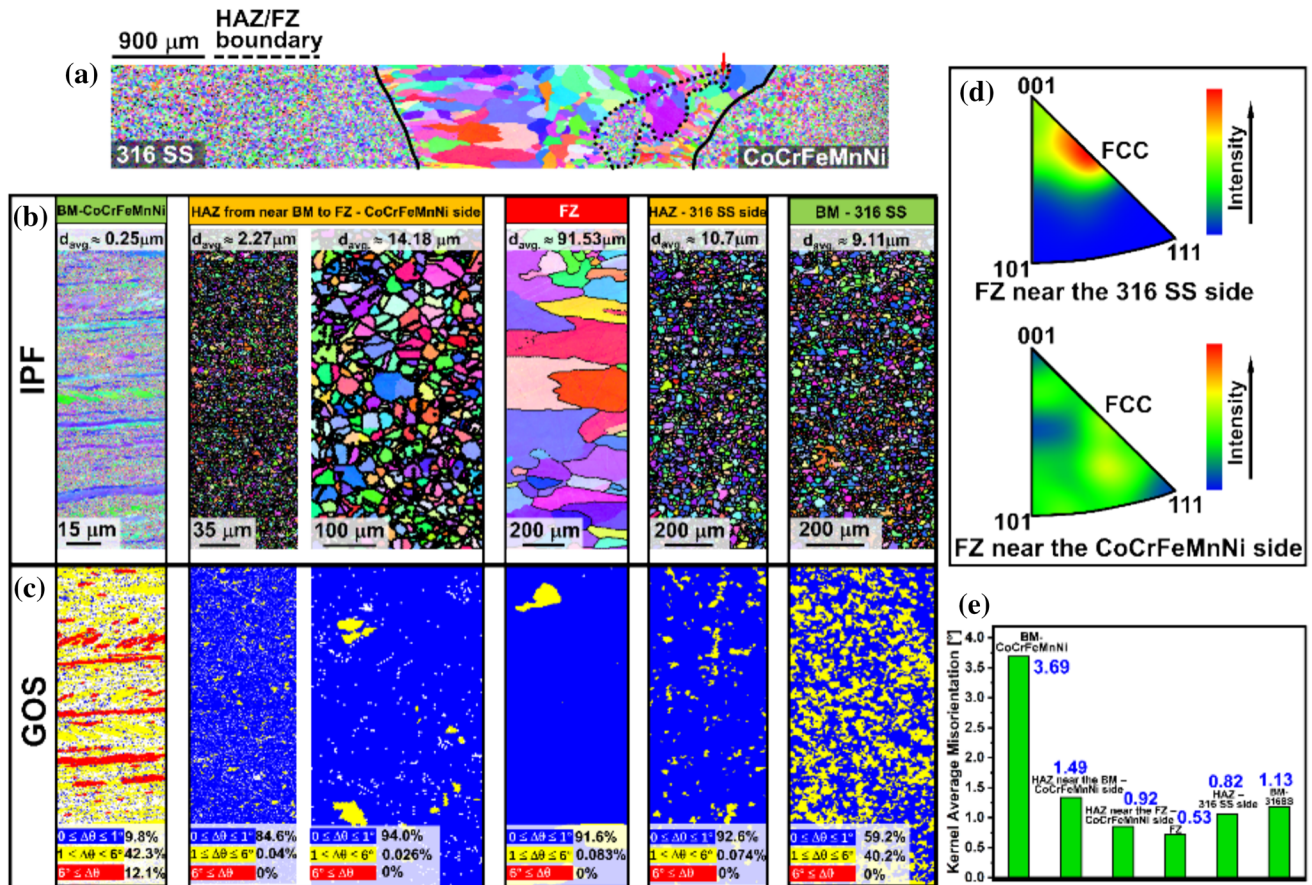
Figure 4 **a**: EBSD map across the dissimilar welded joint; **b** and **c**: IPF and GOS (from left to right) of the CoCrFeMnNi BM, HAZ on the CoCrFeMnNi side, FZ, HAZ on the 316SS side and 316SS BM, respectively. **d**: Texture map; **e**: KAM values with respect to the different regions of the joint.

the CoCrFeMnNi HEA and stainless steel. Moreover, it confirms that the selected welding parameters enable defect-free and fully penetrated welded joints. Additionally, attention is drawn to the peninsula-shaped region enclosed by black dashed lines in Fig. 4a, which corresponds to the previously mentioned macrosegregation region. Upon closer examination, the macrosegregation region in Fig. 4a exhibits a crystal structure morphology distinctly different from the large columnar crystals formed in the surrounding bulk weld metal. Further, the observed macrosegregation region of Fig. 4a presents fine equiaxed grains, attributed to the relatively higher liquidus temperature of the stainless steel BM compared to the bulk weld metal ($T_{L-316SS\ BM} \approx 1454°C$ vs. $T_{L-FZ\_B} \approx 1421\ °C$) and a smaller solidification temperature range ($\Delta T_{L-316SS\ BM} \approx 40\ °C$ vs. $\Delta_{TL-FZ\_B} \approx 61\ °C$). The rapid solidification of stainless steel leads to the formation of fine equiaxed grains. This is the result of substantial undercooling

and the inherent higher cooling rate of this material portion upon integration into the bulk weld metal due to convective effects.

Attention is now directed toward the crystallographic evolution in different regions (BM, HAZ, and FZ) of the CoCrFeMnNi-stainless steel dissimilar welded joint. Figure 4b and d, respectively, illustrates the inverse pole figure (IPF) and grain orientation spread (GOS) maps for the CoCrFeMnNi side of the joint, including the BM, HAZ, and FZ, as well as the IPF and GOS maps for the stainless steel side in the BM and HAZ.

Firstly, from the IPF map presented in Fig. 4b, the influence of the weld thermal cycle on the microstructure within the joint is apparent. The previously pancake-shaped and highly deformed grains in the as-rolled CoCrFeMnNi BM are gradually replaced by equiaxed grains under the influence of the weld thermal cycle. Additionally, the grain size increases

progressively, from ≈0.25 μm (in the CoCrFeMnNi BM) to ≈2.27 μm (near the CoCrFeMnNi HAZ), eventually reaching approximately 14.18 μm (when approaching the FZ from the CoCrFeMnNi side). The phenomena of grain recovery, recrystallization, and grain growth in the as-rolled CoCrFeMnNi BM under the weld thermal cycle were expected. This is primarily driven by the release of strain energy stored in the highly plastically deformed CoCrFeMnNi BM prior to welding, aiding in the development of the observed solid-state phase transformations triggered by the weld thermal cycle. The heat input and prolonged high-temperature duration of the weld thermal cycle provide sufficient driving force similar to low/high-temperature annealing treatments enabling the occurrence of those solid-state phase transformations.

Further observation of the evolution of recrystallization degree in the as-rolled CoCrFeMnNi BM due to the process thermal cycle is shown in Fig. 4c from the GOS maps. From Fig. 4c, it can be observed that in the HAZ on the CoCrFeMnNi side, the closer to the heat source, i.e., the longer the peak temperature and high-temperature duration, the lower the GOS values, which fall within the 0 to 1° range (GOS$_{BM}$ ≈9.8% vs. GOS$_{HAZ\ near\ the\ BM}$ ≈84.6% vs. GOS$_{HAZ\ near\ the\ FZ}$ ≈94.0%). This indicates that recrystallized grains gradually replace deformed grains, aligning with the occurrence of solid-state phase transformations as deduced from the changes in grain morphology. When entering the FZ (refer to Fig. 4a, remarkably large grains were observed near the HAZ/FZ boundary on the side adjacent to 316 stainless steel side, measuring approximately ≈91.53 μm. These columnar grains follow an outward growth pattern originating from the cold substrate of the HAZ and extending toward the center of the FZ. According to metal solidification theory, grain growth typically occurs along the direction of the maximum temperature gradient perpendicular to the liquid/solid interface [38]. Here, a cold substrate favors grain nucleation, leading to the formation of small equiaxed grains. However, as solidification progresses toward the joint centerline, competitive growth occurs. Therefore, in the FZ, a phenomenon is usually observed where small equiaxed grains transform into larger columnar grains that preferentially grow perpendicular to the HAZ/FZ boundary. In contrast, near the HAZ/FZ boundary on the CoCrFeMnNi side, the grain structure exhibits a refinement (refer to Fig. 4a). This refinement can be primary attributed to the composition of the macrosegregation region and

strong fluid flow, leading to a faster cooling rate (refer to C region marked in Fig. 4b and c). The HAZ/FZ boundary on the side of CoCrFeMnNi acting as a cold substrate provides nucleation sites for grain formation. Additionally, peninsula-shaped macrosegregation regions form near the CoCrFeMnNi side of the FZ/HAZ boundary, impeding the competitive growth path toward the center of the joint on the CoCrFeMnNi side. Therefore, only small equiaxed grain structures are observed near the CoCrFeMnNi side of the HAZ/FZ boundary. Furthermore, within the FZ, the grains exhibit different preferred growth orientations near the stainless steel side and the CoCrFeMnNi side (refer to Fig. 4d). Specifically, grains near the CoCrFeMnNi side do not show a clear preferred growth orientation. However, at the HAZ/FZ boundary near the stainless steel side, most grains preferentially grow along the (114) direction, deviating by 3.37° from the (001) direction, indicating the inhibition of growth along the (101) and (111) directions due to competitive grain growth mechanisms during solidification.

Regarding the degree of grain deformation within the FZ, it can be observed from the distribution of the GOS values (see Fig. 4c) that the local deformation of the entire weld joint is relatively low. From the 316 stainless steel BM to the HAZ on the same side under the influence of weld thermal cycle, the change in average grain size was not significant, increasing from approximately ≈9.11 μm to about ≈10.70 μm. Additionally, upon examining the distribution of the GOS values, it is noted that the proportion of GOS values within the 0 to 1° range is ≈59.2%, further increasing to ≈92.6% upon entering the FZ on the stainless steel side. However, the deformation of grains in both the 316 stainless steel BM and its adjacent HAZ is relatively small. This is because this BM is in the annealed state prior to welding. After undergoing annealing treatment, most of the lattice distortion and strain energy within the grains of the stainless steel BM are released. Therefore, despite sufficient heat input is provide to the material during the weld thermal cycle, the stainless steel BM itself lacks strain energy as a driving force for noticeable changes in the grain size and internal strain within the HAZ.

KAM maps showcase the average misorientation between all neighboring pixels, providing a quantitative assessment of local strain. Figure 4e presents the KAM values for the different regions within the CoCrFeMnNi-stainless steel dissimilar welded joint. As expected, the highest KAM value (≈3.69°) is observed
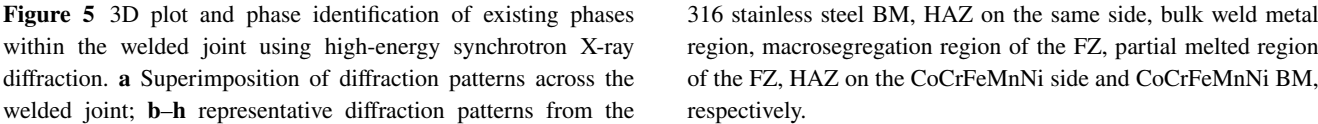
in the as-rolled CoCrFeMnNi BM. Moving toward the FZ boundary on the CoCrFeMnNi side, the KAM value decreases to ≈0.92°. This trend aligns with the evolution of GOS values (refer to Fig. 4c), indicating a reduction in dislocation density and internal strain energy. This further confirms that the primary driving force for solid-state phase transformation occurs in the CoCrFeMnNi HAZ. The lowest observed KAM value in the FZ is approximately ≈0.53°. Furthermore, in the BM and HAZ of the 316 stainless steel side, relatively low KAM values of about ≈0.82° and ≈1.13°, respectively, are observed. This is mainly attributed to the annealing process undergone by this BM prior to welding, which releases most of the lattice distortions and strain energy. Overall, the changes in KAM values are closely associated to the evolution of strain distribution during welding, providing quantitative information for the study of local microstructure changes in the CoCrFeMnNi-stainless steel joint dissimilar welded joint.

High-energy synchrotron X-ray diffraction (SXRD), as a nondestructive testing technique, operates in transmission mode and offers advantages such as high photon flux and rapid data acquisition. These exceptional features empower this characterization technique to reveal detailed changes in micro- to mesoscale structures, accurately identifying minority precipitates and nanoscale phases. In contrast, traditional characterization techniques such as laboratorial X-ray diffraction, struggle to effectively discern these microstructural changes, particularly in identifying minority nanoscale phases. Given the complex conditions of the FZ within the non-equilibrium solidification of the dissimilar welded joints and understanding how the weld thermal cycle influences microstructural changes, especially potential nanoscale precipitate phases in the FZ, is of paramount importance since it can drastically impact mechanical performance. Hence, SXRD is utilized to identify the existing phases in the welded joints, starting from the stainless steel, traversing through the HAZ and FZ, and ultimately reaching the CoCrFeMnNi BM. In the stacked diffraction patterns of the entire dissimilar welded joint, as shown in Fig. 5a2, the red and blue lines represent the boundaries between FZ/HAZ and HAZ/BM, respectively. Representative diffraction patterns for each typical region and the corresponding phase identification results are illustrated in Fig. 5d–h.

It is important to note that Fig. 5b, c, g and h correspond to the stainless steel BM, the HAZ on the same side, the HAZ on the CoCrFeMnNi side, and the CoCrFeMnNi BM, respectively. Based on the segregation phenomena identified in the FZ (as determined by OM, EDS, and thermodynamic simulations (refer to Figs. 2h1, 3, 4, respectively), the FZ is divided into three regions for the study of the phase structure evolution, as illustrated in Fig. 5a1. In this representation, A, B, and C denote the bulk weld metal, the macrosegregation region, and a portion of the partially melted zone in the FZ, respectively. The SXRD diffraction spectra and phase identification results for these three regions are detailed in Fig. 5d, e and f, respectively, confirming the existence of distinct phase structures across the different regions that formed in the welded joint (refer to Fig. 5b–h).

The subsequent analysis will focus on different regions of the welded joint, starting with two BMs used for dissimilar welding. Examining the X-ray diffraction pattern corresponding to the 316 stainless steel BM (refer to Fig. 5b) diffraction peaks for FCC austenite (γ) and BCC ferrite (δ) phases, as well as the intermetallic σ phase, is identified. Although 316 stainless steel is an γ-FCC grade, trace amounts of δ-BCC can form depending on its thermomechanical processing. It is noteworthy that the diffraction peak intensity representing the δ-BCC phase is low, indicating that this BM is primarily composed of γ-FCC. The intermetallic σ phase in 316 stainless steels has been a subject of interest. According to existing literature [39], the precipitation mechanism and kinetics of σ phase depend on various factors such as the chemical composition and structure of the austenite phase, annealing conditions, thermomechanical processing type, and aging conditions. Additionally, σ phase tends to precipitate easily, exhibiting rapid precipitation characteristics [40–42]. Furthermore, the presence of the δ-BCC phase has been confirmed to enhance the kinetics of σ phase formation [43–45]. The series of thermomechanical processing (hot rolling, cold rolling, and annealing) that the present 316 stainless steel underwent before welding, justify the low volume fraction (≈1.51%, as determined by Rietveld refinement) of σ phase in BM. Note, for clarity, that the both FCC phases that exist in the CoCrFeMnNi HEA and stainless steel are, respectively, referred to as FCC and γ-FCC phase. The equiatomic CoCrFeMnNi HEA is predominantly composed of an FCC structure (refer to Fig. 5h). However, due to minor elemental contaminations during the fabrication of the cast ingots formation of Cr-Mn-based oxides occurs, as also confirmed by EDS analysis in

Figure 5 3D plot and phase identification of existing phases within the welded joint using high-energy synchrotron X-ray diffraction. **a** Superimposition of diffraction patterns across the welded joint; **b–h** representative diffraction patterns from the 316 stainless steel BM, HAZ on the same side, bulk weld metal region, macrosegregation region of the FZ, partial melted region of the FZ, HAZ on the CoCrFeMnNi side and CoCrFeMnNi BM, respectively.

previous studies [37]. From the present SXRD data, Rietveld refinement was used to calculate the phase volume fraction of these oxides totaling ≈1.35%.

Moving into the HAZ on the CoCrFeMnNi side (refer to Fig. 5g), it is observed that, apart from maintaining trace amounts of Cr-Mn oxides (approximately ≈1.43%), the disordered FCC phase is dominant. This is a typical microstructure of the material after being hot/cold rolled or after relatively short heat treatment schedules. Previously, Kim et al. [46] studied the high-temperature oxidation behavior of the CoCrFeMnNi HEA within the temperature range from 900 to

1100°C, finding that at high temperatures, Cr and Mn have a strong affinity for oxygen, making it easy the formation of oxides enriched in these elements. Thus, the presence of such these oxide phases in the HAZ is not uncommon and possesses a dual origin: from the BM casting and from (minor) oxidation occurring during welding. Similarly, in the HAZ of the stainless steel BM no new phases were formed (refer to Fig. 5d) and the phase volume fractions remain almost consistent with those of the BM, suggesting the increased heat resistance of this material as well as slower transformation kinetics to the experienced thermal cycle.

For 316 stainless steels heat treatments can easily promote the transformation of δ-BCC to σ, especially when the temperature is maintained a 950°C and above. Although these temperatures are achieved in the HAZ, the rapid cooling rate and insufficient peak-temperature holding time are not conducive to further transformation δ-BCC to σ.

Although both BMs used for dissimilar welding are primarily composed of the FCC phase, their mixing in the FZ alters the overall chemical composition of this zone, thereby potentially influencing the solidification structures. The FZ is divided into three regions based on the measured elemental distribution: the bulk weld metal region, macrosegregation region, and partially melted region, as previously shown in Fig. 5. Figure 5d, e and h depicts representative X-ray diffraction patterns for these regions. Comparison of the phase identification results for these three regions reveals distinct phase structures due to chemical composition variations. In the bulk weld metal region (Fig. 5d), a well-mixed area of the two BM components is observed, with four-phase structures being detected. In addition to the FCC matrix phase that is composed of both BMs, the bulk weld metal region also shows evidence of a BCC phase, Cr-Mn oxides, and σ phase. Despite the use of Ar inert shielding gas protect both the top and bottom surfaces of the welded specimen, nucleation of Cr-Mn oxides still occurs (Fig. 5d), which is attributed to the large heat source size and potential gas turbulence during welding. The presence of oxide particles is common in arc-based welding processes of this HEA system, highlighting the difficulty in avoiding even minor oxygen absorption by the CoCrFeMnNi HEA and oxide formation at high temperatures. Similar oxide particles have been detected in previous dissimilar welded joints of CoCrFeMnNi with 308 and 410 stainless steel grades [37, 47]. Although the volume fraction (approximately ≈1.67%) is slightly higher than that in the BM and the HAZ, it does not negatively affect the mechanical properties of the joint.

Regarding the formation of the BCC phase, BCC ferrite is typically formed during the solidification process for most austenitic stainless steel [48], with its phase fraction being dependent on both composition and cooling conditions. Complete dissolution of this BCC phase is challenging, but its presence is beneficial in preventing issues as hot cracking and segregation during welding [48]. In previous studies, rapid prototyping techniques such as laser [49, 50], electron beam [51], and arc-based welding [52] have been used to manufacture austenitic stainless steel components. These components exhibit a microstructure consisting of γ-FCC austenite and δ-BCC ferrite under high cooling rate processes. According to the present synchrotron data results, the volume fraction of this phase calculated by Rietveld is approximately ≈3.94%. Compared to the volume fraction of the BCC phase in the stainless steel BM (≈3.44%) and the HAZ (≈2.54%), there is a slight increase, suggesting that upon the change in chemistry of this zone the solidification and transformation kinetics of this phase are lower. As for the formation of σ phase (volume fraction of ≈1.02%), generally, this phase structure is formed during the aging process at temperatures ranging from 500 to 800 °C. However, in this dissimilar welded joint, its presence is attributed to the segregation of both Cr and Mo that exist on the 316 stainless steel BM [53], increasing the probability for the formation of the Mo-rich σ phase in the FZ. Previous work by Qing et al. [54] delved into the impact of adding Mo on the microstructure evolution in CoCrFeMnNi HEA, revealing that the addition of this element can aid the formation of Mo-rich σ. Furthermore, the presence of Cr from both BM in the FZ also aids in contributing to the formation of σ phase. According to thermodynamic simulations (refer to Fig. 4), the BCC phase is enriched in Fe and Cr, while Cr, Fe, and Mn enriched σ phase. The dilution ratio between the two BMs in the FZ will then have a significant impact on the potential formation of BCC and σ phases.

Figure 5e details the phase identification for the macrosegregation region within the FZ, indicating that the phase structure observed aligns with that previously observed in the bulk weld metal (refer to Fig. 5d), encompassing FCC, BCC, σ phase, and Cr-Mn oxides. The primary discrepancy lies in the volume fraction of existing phases. Drawing from the thermodynamic analysis conducted earlier, the macrosegregation region (refer to Fig. 5a1, region D) arises from the preferential melting of the stainless steel at high-temperature conditions ($T_{L\text{-}316SS\text{-}BM} > T_{L\text{-}FZ}$), followed by rapid solidification induced by convection in the molten pool. The swift solidification in this region results in a higher cooling rate compared to the solidification rate in the bulk weld metal region, explaining the disparity in the amount of BCC phase precipitation between the macrosegregation and the bulk weld metal region. According to the Rietveld refinement results, the volume fraction of the precipitated BCC

phase in the macrosegregation zone is slightly lower than that in the bulk weld metal region (≈2.79% vs. ≈3.94%). This can be ascribed to the rapid non-equilibrium solidification in this region, which restricts the amount of BCC phase precipitation. Regarding σ phase, its formation typically involves prolonged high-temperature aging processes. However, it is noteworthy that σ formed in the rapidly cooled macrosegregation zone. Previous literature outlines two ways of σ phase formation [55, 56]: eutectoid decomposition, where BCC phase decomposes into σ and FCC phases during fast cooling, and nucleation and growth of σ phase from the BCC phase, with Cr-rich elements in the BCC phase acting as nucleation sites for the σ phase. Under normal aging conditions, the decomposition of BCC phase into σ phase and FCC phase

necessitates at least 0.5 h of aging at 700 °C. Although theoretically σ phase should not appear in the rapidly solidified FZ, its presence in the molten pool implies that the rapid cooling in the macrosegregation region caused localized segregation, in particular Cr, which facilitated the formation of σ phase despite the high cooling rates.

The final analyzed region encompasses the partially melted zone within the FZ as illustrated in Fig. 5f). SXRD phase identification revealed the presence of three distinct phase structures in this region, namely FCC, σ phase, and Cr-Mn oxides. Interestingly, no traces of the BCC phase were found in this region. This absence suggests that the Fe content from the stainless steel BM (refer to Fig. 6d2) might not be enough to promote the formation of the BCC phase
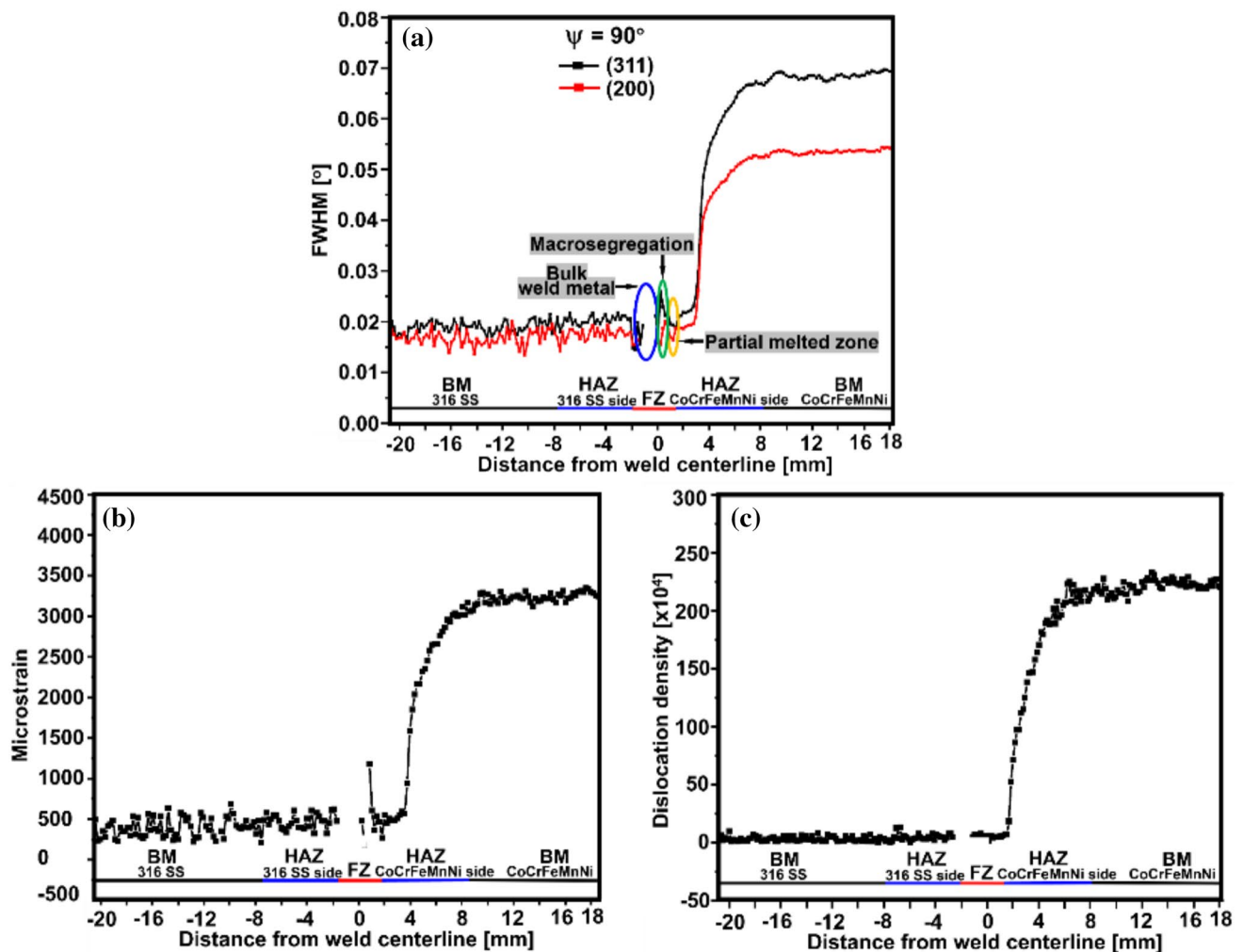

Figure 6 **a**: evolution of the FWHM for the dissimilar welded joint considering the (311) and (200) diffraction peaks near the 90° azimuthal angles. **b** and **c**: Evolution of joint microstrain along the longitudinal direction.

in this particular partially melted zone, highlighting how dilution effects can significantly impact the phase structure evolution. Furthermore, the presence of σ phase in this region challenges the previously established understanding of the interdependence between σ and BCC phases in the FZ. As detailed before, for stainless steels the formation of σ phase was linked to the presence of the BCC phase. However, in this partially melted zone, the formation of σ phase appears to be independent of the decomposition or nucleation and growth of the BCC phase. This emphasizes that, under specific conditions, the formation of different phases may be influenced by factors beyond conventional thermodynamics and phase transition kinetics. Additionally, by comparing the liquidus temperature and the solidification temperature range obtained previously through previous thermodynamic calculations for the FZ (refer to Fig. 4d), reveals that, among the three distinct regions in the FZ (refer to Fig. 4a1), the liquidus temperature is lowest, and the solidification temperature range is widest in the partially melted zone D. This implies that the occurrence of the σ phase may be related to a relatively large solidification temperature range, indicative of a potentially slower solidification rate. The volume fractions of existing phases exist in each region are summarized in Table 1.

In conclusion, the entirety of the FZ, encompassing the bulk weld metal zone, macrosegregation zone, and partially melted zone, experiences the formation of BCC and σ phases primarily due to compositional disparities resulting from the dilution ratio between the two BMs used in this work. This compositional contrast, coupled with the presence of FCC and Cr-Mn oxide particles, gives rise to distinct solidification behaviors.

To gain further insights into microstructural evolution, further analysis of the SXRD raw data was performed to evaluate how full width at half maximum (FWHM), microstrain, and dislocation density evolves across the joint. Figure 6a, b and c, respectively, details the analysis of the: (i) evolution of the FWHM considering the (311) and (200) diffraction peaks, (ii) microstrain along the vertical weld direction, (iii) and dislocation density. The methodology used for the calculation of microstrain and dislocation density is comprehensively detailed in [57] and is not reiterated here. Of importance, it is critical to detail the microstrain calculations, and the Debye–Scherrer rings were integrated around the 90° angle, corresponding to the vertical weld direction ($\varphi = 90°$). Starting with Fig. 6a, it is evident that the FWHM values exhibit no significant change from the stainless steel side (both on the BM and HAZ), remaining nearly constant. This stability is primarily attributed to the high-temperature annealing undergone by the material prior to welding, diminishing the thermal impact, i.e., thermally induced residual stresses, on this side of the joint. It is noteworthy that the three primary factors influencing FWHM changes are grain size, microstrain, and dislocation density. Larger grain sizes contribute to smaller FWHM values, and smaller microstrain and dislocation density also lead to reduced FWHM values. The trends in microstrain (refer to Fig. 6b) and dislocation density (refer to Fig. 6c)) on the stainless steel side of the joint closely mirror the evolution of FWHM, confirming that no major microstructure changes occurred due to the weld thermal cycle.

Subsequently, in the macrosegregation region (green ellipse in Fig. 6a), an increasing trend in FWHM values is observed, reaching a peak of approximately ≈0.03°. This increase can be attributed to the rapid solidification of the macrosegregation region due to its smaller solidification temperature range, resulting in the formation of smaller equiaxed grains (refer to Fig. 4a). In the partially melted region (yellow ellipse of Fig. 6a), a decreasing trend in FWHM values is observed. This is related to the columnar grains formed in this region, which are smaller than

**Table 1** The summed volume fraction of phases exists in each region

	FCC	BCC	σ	Cr-Mn oxide
BM: 316 stainless steel	≈95.05%	≈3.44%	≈1.51%	–
HAZ: 316 stainless steel side	≈95.95%	≈2.54%	≈1.51%	–
FZ: Bulk weld metal	≈93.37%	≈3.94%	≈1.02%	≈1.67%
FZ: Macrosegregation	≈94.33%	≈2.79%	≈1.21%	≈1.67%
FZ: Partial melted zone	≈97.20%	≈1.13%	–	≈1.67%
HAZ: CoCrFeMnNi HAZ side	≈98.57%	–	–	≈1.43%
BM: CoCrFeMnNi HAZ	≈ 98.65%	–	–	≈ 1.35%

those in the bulk weld metal area, although larger than those observed in the macrosegregation region (refer to Fig. 4a). Detailed comparisons of grain sizes in these three regions are shown in Fig. 4d. Finally, upon entering the CoCrFeMnNi side of the joint, it is possible to observe that the largest FWHM values are observed in the BM region. This is attributed to the high plastic strain generated by the rolling process of the CoCrFeMnNi BM prior to welding, while in the HAZ the weld thermal cycle promoted a softening effect, efficiently decreasing the defect density and translating into a lower FWHM, microstrain and dislocation density compared to the rolled BM. The trend in dislocation density obtained from SXRD in Fig. 6c is similar to the trends in KAM values obtained from EBSD data, confirming the combined effect of previous thermomechanical processing and weld thermal cycle experienced by the materials to be joined. Furthermore, a comparison of the microstrain in the two base materials reveals that the microstrain in the CoCrFeMnNi high-entropy alloy side is significantly higher than that in the 316 stainless steel side. This difference can be attributed to the processing histories of the two base materials prior to welding. Specifically, the direct influencing factor for microstrain is dislocation density. In this study, the CoCrFeMnNi

base material underwent cold rolling before welding, which introduced considerable plastic deformation, significantly increasing lattice defects and internal stresses. Conversely, the 316 stainless steel base material underwent high-temperature annealing prior to welding, effectively reducing the dislocation density and residual stresses. Consequently, the cold rolling process markedly increased the microstrain of the CoCrFeMnNi base material, while the annealing process significantly reduced the microstrain in the 316 stainless steel base material, resulting in the observed differences in microstrain levels between the two materials.

To replicate the non-equilibrium solidification conditions and phase structure evolution of the dissimilar welded joint, Fig. 7 illustrates the predicted solidification curves for the three distinct locations (region A, macrosegregation region B and partially melted region C, as shown in Fig. 7a1) observed in the FZ using the Scheil–Gulliver model. Considering the elemental redistribution in the FZ due to complex mixture of elements and the preferential loss of certain elements through evaporation, adjustments to the nominal starting composition of the alloy were made to predict solidification behavior of the FZ more accurately. This was performed using multiple composition

Figure 7 **a1**: overview of cross section of the welded joint; **a2**: average composition from EDS analysis of regions **A**, **B**, and **C**, as marked in **a1**; **b**, **c** and **d**: Scheil calculations performed considering the average composition from the EDS analysis.
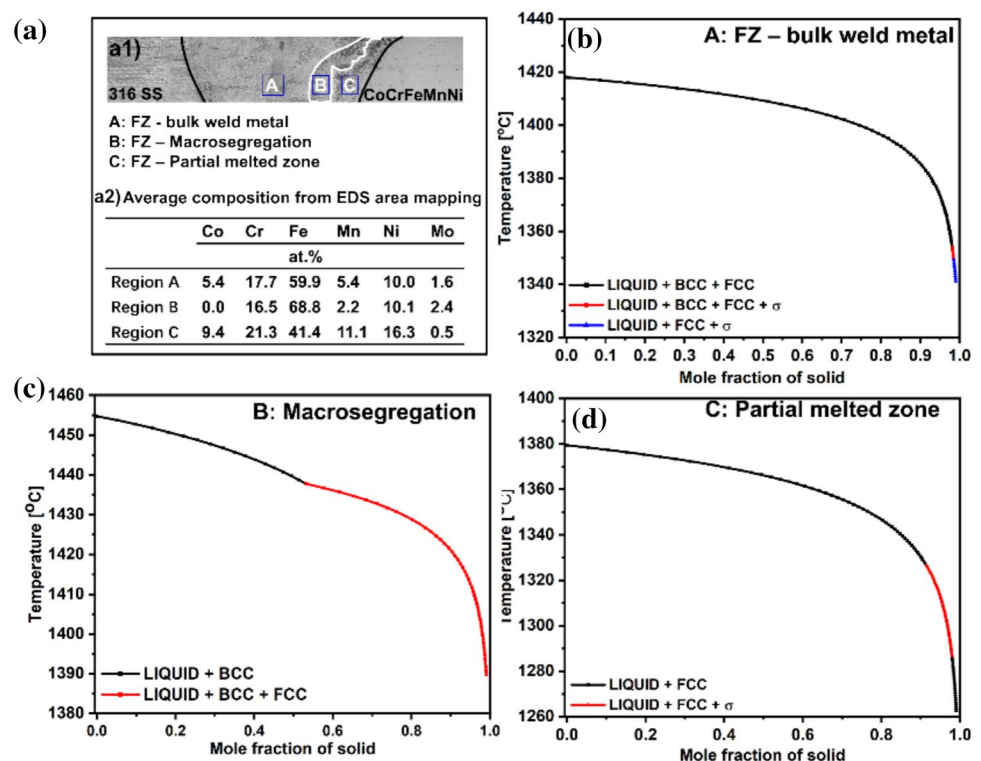
measurements at each location to obtain a reliable average value that could be used for the calculation. The average compositions of the three representative regions in the FZ, are presented in Table of Fig. 7a. Notably, these three regions exhibit distinct solidification paths (refer to Fig. 7b, c, and d), primarily due to variations in composition distribution among them (refer to Fig. 7a2), which are discussed next.

In the bulk weld metal region, depicted in Fig. 7b, the Scheil–Gulliver model was utilized to forecast the solidification path, encompassing three key stages. Initially, the transition from the liquid phase to a coexistence of FCC and BCC phases occurred. Then, σ starts to form alongside with FCC and BCC. Lastly, the solidification finished with only FCC and σ remaining in the last liquid to solidify. Thus, according to these calculations the solidified material in the bulk weld metal region should be composed of FCC, BCC, and σ phases. These thermodynamic predictions are validated by the previously reported SXRD data (refer to Fig. 5d). However, the calculations failed to predict the existence of the observed Cr-Mn oxides in the bulk weld metal region. This is because such thermodynamic calculations do not consider oxidation processes, while such phenomena are widely prevalent in arc-based welding. Nevertheless, since we know the oxide fraction prior (≈1.35%) and after welding in the HAZ and FZ (≈1.43 and ≈1.67%) we can assess how the weld thermal cycle contributes to oxidation at each location of the joint. It should be noticed that the change in oxide fraction is relatively low since inert shielding gas was used to protect the thermally affected regions during the high-temperature processing employed in this work. Here, it is worth emphasizing that despite the recognized limitations of the Scheil–Gulliver model in simulating oxidation reactions, synchrotron radiation data have validated the presence of these Cr-Mn oxides (as shown in Fig. 5). This finding indicates that although the model does not directly predict the oxidation process, the phase identification experimental results provide strong assessment and verification of the actual oxidation effects. Besides, as demonstrated in this work, this existence of weld thermal cycles and their effects on welded joints are achieved through various indirect experimental data. Future work will employ thermocouples for real-time temperature measurement and numerical simulations to further quantify the thermal cycle characteristics, thus strengthening direct evidence.

Attention is now turned to macrosegregation region B, as depicted in Fig. 7a1. In alignment with the preceding analysis, the composition within this region closely mirrors that of the stainless steel BM (refer to Fig. 7a2). The solidification trajectory and resultant phase structure in this zone are illustrated in Fig. 7c. From the associated Scheil solidification path, it is revealed that non-equilibrium solidification leads to a phase structure comprising both BCC and FCC phases. The BCC phase predominantly forms from the liquid, followed by simultaneous formation of both FCC and BCC phases at the last stage of solidification. However, in contrast to that measured using SXRD, the presence of the observed σ phase in the macrosegregation region was not accurately predicted by. As discussed in the earlier section analyzing the SXRD data, the σ phase observed in the macrosegregation region deviates from conventional precipitation principles, and its formation may be linked to the decomposition, nucleation, and growth of BCC. It is important to note that thermodynamic calculations can face challenges in precisely predicting this solidification phase structure in multicomponent alloys. This difficulty may stem from the inherent complexities in forecasting microscale dynamics, such as nucleation and growth, during phase transitions in complex alloy systems. Furthermore, the rapid non-equilibrium solidification in this region might introduce microscale non-uniformities, contributing to uncertainties in the thermodynamic simulation condition.

Finally, we consider the evolution of the partially melted region C (refer to Fig. 7d). In this region, the solidification path undergoes two steps: liquid → liquid + FCC, followed by the formation of FCC and σ phase in the remaining liquid. The SXRD data of this region confirms the validity of these predictions, by accurately detecting both FCC and σ phases. This reiterates that the Fe content in the partially melted region C is insufficient to induce the precipitation of the BCC phase, which tends to be enriched in Fe and Cr, highlighting how the complex mixing of multiple elements in dissimilar welded joints can bring intricate phase structures depending on the local composition, mixing and solidification conditions.

Mechanical properties

To determine how the local microstructure impacts the micro- and macromechanical behavior of the joints, multiscale mechanical characterization was

performed. The joint microhardness mapping is shown in Fig. 8a, clearly identifying the different regions of the joint. The microstructural variations within different regions of the welded joint can affect the local microhardness, as evident in Fig. 8b. The CoCrFeMnNi BM displays the highest hardness at 410 HV0.5, stemming from its cold worked microstructure. Upon entering the HAZ on the CoCrFeMnNi HEA side, a softening behavior is observed, leading to a decrease in hardness from ≈410to ≈150 HV0.5. This reduction is attributed to solid-state phase transformations occurring during the weld thermal cycle, akin to low/high-temperature heat treatment that developed due to the weld thermal cycle. The HAZ experiences recovery, recrystallization, and grain growth in the previously highly deformed CoCrFeMnNi BM. According to the Hall–Petch, the growth of previously small grains contributes to the decrease in material hardness. The extent of solid-state phase transformation that occur in the HAZ is dependent on the distance to the heat source, with the trend of hardness reduction being steeper near the FZ, due to the existence of larger grains.

The FZ's hardness variation is marked by three regions: the partially melted region, macrosegregation region, and bulk weld metal region, denoted by yellow, green, and black solid ellipses, respectively. Microstructural illustrations of these regions are

Figure 8 a: Microhardness map across the welded joint; **b**: microhardness profile obtained along the black line of the **a**.

provided in the insets of Fig. 8b. Comparing hardness values, the macrosegregation region exhibits the highest hardness due to small equiaxed grains formed owing to the high solidification rate. In contrast, the bulk weld metal region which features large columnar grains, and the partially melted region are smaller. According to the Hall–Petch effect, the smaller grains in the partially melted zone should increase the hardness. However, due to the complete dissolution of the hard BCC phase in this region (refer to Fig. 5f), the final hardness value is similar to that of the bulk weld metal region. Moving into the stainless steel BM and its adjacent HAZ, no significant changes in hardness values are observed, remaining at approximately ≈175 HV0.5. This stability is attributed to the high-temperature annealing treatment undergone by this BM before welding. The imposed pre-welding annealing treatment prevents significant alterations in microstructure, grain size, or microstrain in these regions, resulting in relatively constant hardness values. Here, it is important to note that considering the numerous challenges that high-temperature annealing might face in actual industrial production environments, future work will focus on investigating the mechanical properties of the 316 stainless steel BM used in welded joints without high-temperature annealing.

To assess the suitability of these dissimilar joints to be considered for structural applications, tensile testing was performed. Figure 9 provides representative tensile stress–strain curves that elucidate the mechanical performance of these dissimilar joints, obtained through two distinct welding methods: GTAW (current work) and laser welding [32]. The assessment also encompasses the mechanical properties of the two base materials, with Table 2 summarizing their performance metrics, including ultimate strength and elongation. The combined analysis of Fig. 9a and Table 2, detail that the welded joints, while exhibiting lower ultimate strength and ductility compared to the original base materials, still manifest high mechanical performance, hinting at their potential for structural applications. Notably, a comparative analysis of these dissimilar joints obtained by GTAW and laser welding showcases that the former exhibits superior mechanical performance. Specifically, in terms of strength, the dissimilar joints obtained with GTAW slightly outperform those the laser-welded one (≈495 vs. ≈459 MPa, respectively). Moreover, in terms of elongation, the laser joints only had half the elongation of those under GTAW counterparts (≈5.0% vs
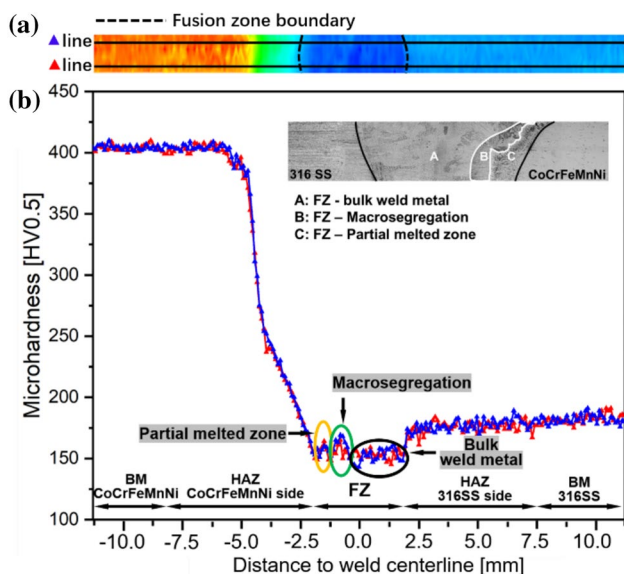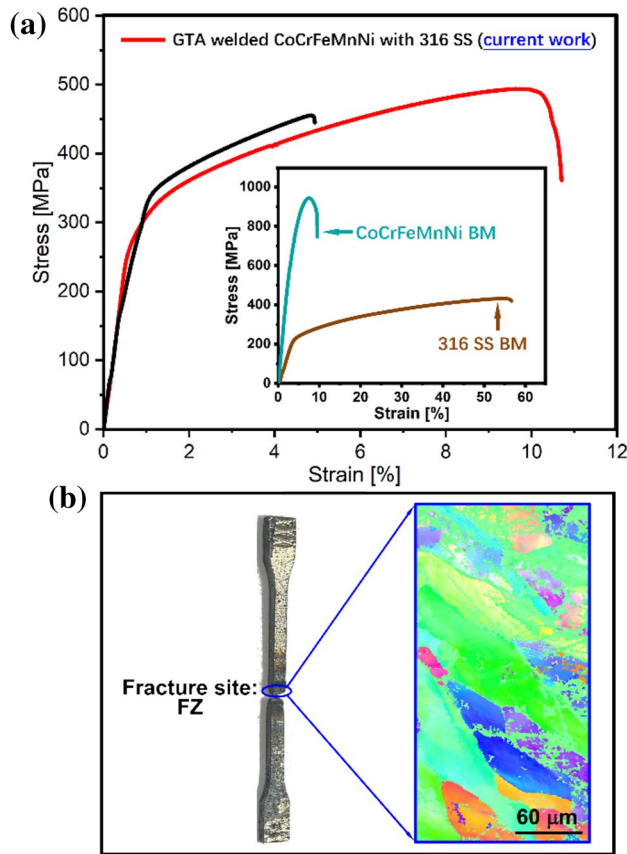
Figure 9 a Representative stress–strain curve of the GTAW CoCrFeMnNi-316 stainless steel dissimilar joints, the inset detail the representative stress–strain curves of the BMs used; **b** the fractured specimen with EBSD Inverse pole figure maps near the fracture site.

Table 2 Summary of the base materials and welded joints mechanical properties

	Ultimate strength	Fracture strain
	[MPa]	[%]
CoCrFeMnNi BM [32]	≈ 948	≈ 9.5
316 stainless steel BM [32]	≈ 431	≈ 56.8
Laser-welded joint [32]	≈ 449	≈ 5.0
GTAW joint (present work)	≈ 493	≈ 10.7

≈10.7%, respectively). A potential explanation for the improved mechanical response of the arc-based joints over the laser-welded ones may be related to the less abrupt microstructure changes: While in laser welding there is a sudden microstructure change from the BM, to the HAZ and the FZ, in arc-based welding the larger heat source introduces a less several microstructure

gradients which can render an improved microstructure and mechanical compatibility upon tensile loading. Besides, larger effective cross-sectional area in the FZ of GTA-welded joint was also the main reason: The FZ is a soft domain with large grain size and lower hardness, affecting stress distribution and deformation. The FZ in GTA-welded joints has a larger effective cross-sectional area compared to laser-welded joints. During tensile deformation, the stress first concentrates in the soft domain and the larger effective cross-sectional area means that under tensile loads the FZ in GTA-welded joints takes longer to yield and undergo plastic deformation. Conversely, the smaller FZ in laser-welded joints experiences higher stress per unit area, leading to yield and plastic deform sooner. Consequently, GTA-welded joints generally exhibit better ductility than laser-welded joints.

Based on the examination of the macroscopic features of the fractured joint surface and observing the presence of coarse columnar grains near the fracture site from EBSD inverse pole figure maps (refer to Fig. 9b), it is evident that the failure occurred in the FZ. Fracture analysis suggests that the primary causes of failure in this region can be attributed to three factors: influence of large columnar grains; presence of a macrosegregation region; and formation of hard secondary phases. Although the ultimate tensile strength (UTS) of the 316 stainless steel base material is relatively low, fracture was expected to occur in the base material. However, the fusion zone exhibited more complex microstructural features compared to the 316 stainless steel base material, which made the fusion zone the weakest part of the entire weld joint and ultimately led to fracture occurring in this region. Specifically, the large columnar grains present in the FZ make it as the area with the lowest hardness within the joint (refer to Fig. 4a). During the tensile process, the load is initially concentrated in the relatively softer FZ, making it the focal point for fracture occurrence. In addition to the large columnar grains, there is also the existence of the already discussed macrosegregation region, which possessed small equiaxed grains. This can lead to a gradient in grain size within the FZ, consequently causing a noticeable hardness gradient affecting the local strength level (refer to Fig. 8). Furthermore, SXRD analysis and thermodynamic simulations have confirmed the presence of BCC and σ phases in the FZ, with particular emphasis on the detrimental σ precipitate phase. This phase has been confirmed to induce premature failure [58]. In numerous literature

reports [37, 49–51] encompassing both similar and dissimilar welding of CoCrFeMnNi, consistent findings indicate that the FZ of the welded joint exhibits the lowest hardness, with fracture consistently occurring in this region. This phenomenon is commonly ascribed to the microstructure within the FZ, specifically the presence of coarse dendritic/columnar grains. The evident presence of such coarse dendritic/columnar grain structures in the FZ significantly detrimentally impacts the mechanical performance of the entire welded joint. Consequently, in future welding processes and joint designs, further efforts to implement measures to enhance the microstructure of the FZ, reduce the formation of coarse dendritic or columnar grains, optimize grain size distribution, and control the generation of undesired secondary phases. This approach will contribute to an overall improvement in the mechanical performance and fracture resistance of the welded joint.

Macrosegregation mechanism

To provide a more detailed explanation of the macrosegregation phenomena within the FZ of the studied dissimilar welded joint, Fig. 10b illustrates the elemental distribution throughout it. Despite the semiquantitative nature of SEM/EDS, the observation of elemental variations within the FZ is still enabled. Figure 10c) presents a distribution curve of the liquidus and solidus temperatures (T_L and T_S, respectively) as determined using the Scheil model and site-specific EDS data, aiming to elucidate the relationship between macrosegregation behavior in the FZ and the solidification temperature ranges (T_L-T_S).

Initially, in both BMs and HAZs, all elements displayed a relatively uniform distribution. This is expected since despite high temperatures are reached, the material remains in the solid state and owing to the relatively short weld thermal cycle, there is not enough time for massive elemental diffusion that could significantly modify the composition of these regions. Analyzing the variation of both liquidus and solidus temperatures (refer to Fig. 10c), it is noticeable that these vary between 1454 (T_L) and 1413 °C (T_S) for the 316 stainless steel BM and between 1345 and 1181 °C, for the CoCrFeMnNi BM. Clearly, the stainless steel BM exhibits a narrower solidification temperature range compared to that of the CoCrFeMnNi HEA BM (41 °C vs. 164 °C). Upon entering the FZ, significant elemental redistribution and macrosegregation
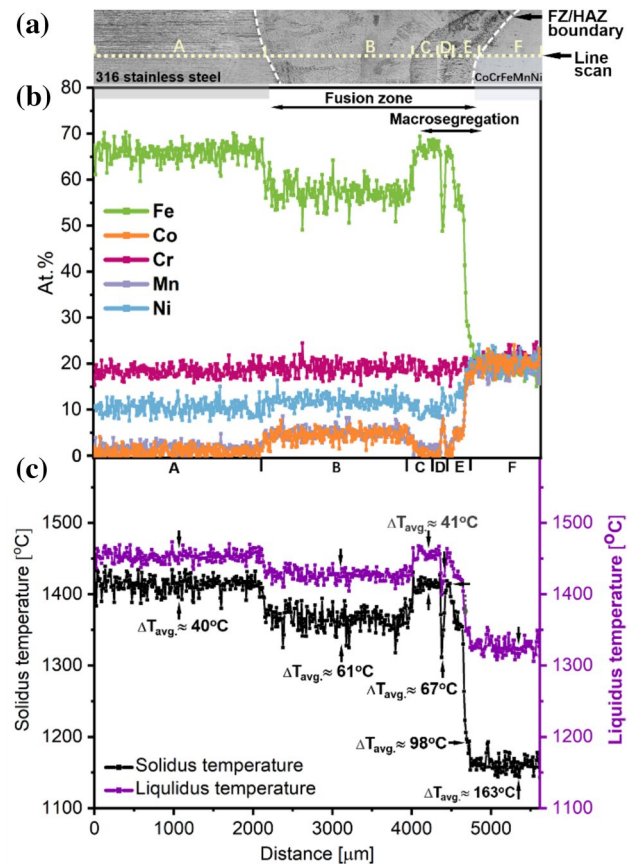

Figure 10 **a**: Overview of the cross section of the dissimilar welded joint; **b**: EDS line scanning across the weld along the blue dashed line of **a**; **c**: solidus (black line) and liquidus (red line) temperature variations.

were observed (refer to Fig. 10b). Based on the compositional differences in the FZ and the inherent characteristics of the two BMs, it can be inferred that the liquidus temperature will be higher or lower than one of the BMs ($T_{L, 316 \text{ stainless steel}}$ and $T_{L, \text{CoCrFeMnNi}}$).

For a clearer comparative analysis, the FZ was divided into four regions: B, C, D, and E, corresponding to the bulk weld metal region (B) and macrosegregation regions (C, D, E), as shown in Fig. 10. First, focus is given to the bulk weld metal region B, the region near the 316 stainless steel side. This region occupies approximately three-quarters of the entire FZ, and the major elements in this region exhibited a relatively uniform distribution, with no evidence of macrosegregation. This indicates that in this region of the FZ, the different elements of the two BMs were well mixed which is corroborated by macroscopic observations of the microstructure. Upon closer inspection, it is observed an enrichment of Fe,

followed by Cr and Ni, and trace amounts of Mn and Co. These elemental distribution characteristics are commonly observed in dissimilar welded joints and can be explained based on the compositional differences of the two BMs. Specifically, the FZ showed an enrichment of Fe and minimal Co content, as expected since the stainless steel BM is rich in Fe but lacks Co. The relatively low Mn content can be attributed to the lower melting and evaporation points of this element, coupled with the high temperatures experienced by the FZ during the welding process, facilitating the preferential loss of Mn.

The liquidus and solidus temperatures and solidification temperature range of the bulk weld metal formed in this region were 1421, 1360, and 61 °C (refer to region B in Fig. 10c), respectively. In comparison with both BMs, these temperatures were lower than that of the stainless steel BM but higher than that of the CoCrFeMnNi HEA BM, i.e., $T_{L\text{-}316SS\ BM} > T_{L\text{-}FZ\_B} > T_{L\text{-}CoCrFeMnNi\ BM}$. Furthermore, they exhibited varying solidification temperature range variation, i.e., $\Delta T_{L\text{-}316SS\ BM} < \Delta T_{L\text{-}FZ\_B} < \Delta T_{L\text{-}CoCrFeMnNi\ BM}$.

Macroscopic segregation, often referred to as beaches, peninsulas, and islands depending on the morphology of the formed regions, is prone to occur in dissimilar welding due to compositional differences between the bulk weld metal region and the BMs, coupled with subsequent changes in local liquidus temperatures. Based on the differential analysis of the solidus, liquidus temperature and solidification temperature ranges between the two BMs and the bulk weld metal in the FZ (region B in Fig. 10c), it is then justified the reason for the observed macrosegregation exists in the CoCrFeMnNi/316 stainless steel joint under study, i.e., a significant difference in liquidus temperatures and solidification ranges in the region of the bulk weld metal (region B) and in the

two BMs, confirming the validity of the observed macrosegregation phenomenon. The occurrence of macrosegregation in the current study is consistent with the conditions reported in previous studies focusing on dissimilar welding [35, 59]: A peninsula or island of the base metal composition can form if $T_{LW} < T_{LB}$ while an irregular-shaped beach of the BM composition can form if $T_{LW} > T_{LB}$ (L_{LW}: liquidus temperature of the bulk weld metal; T_{LB}: liquidus temperature of the BM). Here, it is important to note that the macrosegregation observed in this study is closely tied to fluid flow, particularly the formation of peninsulas (corresponding to region C), which exhibits a composition consistent with the stainless steel BM, on the side closer to the HEA. This is attributed to fluid flow acting opposite to the welding direction, capable of carrying the stainless steel BM the colder regions of the bulk weld metal before solidification, followed by rapid freezing.

Figure 11 provides a comprehensive overview of its underlying formation mechanisms of the macrosegregation observed in the FZ. The liquidus temperature of both the bulk weld metal and BMs plays a pivotal role in the macrosegregation evolution. As depicted in Fig. 10c, the T_L values obtained through ThermoCalc for the two BMs (316 stainless steel and CoCrFeMnNi HEA) and the bulk weld metal are $T_{L,\ 316\ stainless\ steel} \approx 1454°C$, $T_{L,\ bulk\ weld\ metal} \approx 1421°C$, and $T \approx 1345°C$. As previously documented [60], the velocity of the liquid metal must approach zero at the solid–liquid interface, even in the presence of turbulent motion within the molten pool. This condition often leads to the formation of a stagnant layer immediately adjacent to the solid base metal. Consequently, stagnant layers form along the boundaries of both 316 stainless steel and CoCrFeMnNi HEA BMs, followed by melting and solidification during the welding process. Given that $T_{L,\ bulk\ weld\ metal} \approx 1421°C < T_{L,\ 316\ stainless\ steel} \approx 1454°C$,

Figure 11 Summary of macrosegregation mechanisms in dissimilar welding of 316 stainless steel to CoCrFeMnNi HEA, for the formation of peninsulas under the condition of $T_{L,\ bulk\ weld\ metal} < T_{L,\ 316\ stainless\ steel}$, and irregular beaches under $T_{L,\ bulk\ weld\ metal} > T_{L,\ CoCrFeMnNi\ HEA}$.
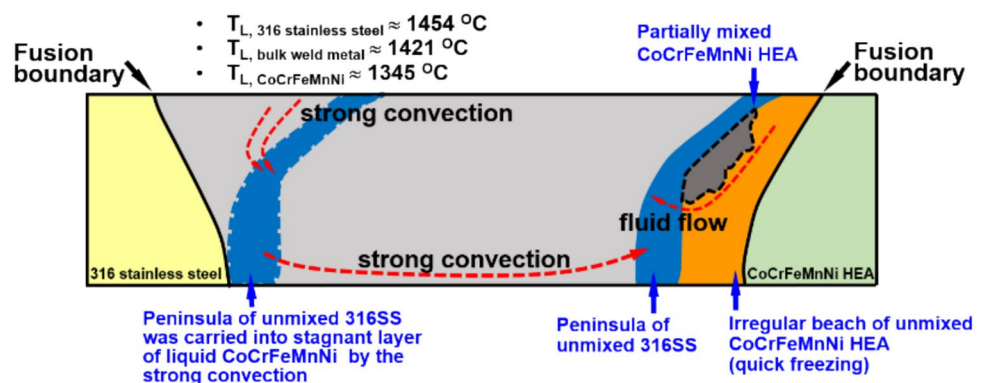
this layer tends to freeze rapidly before mixing with the surrounding liquid. However, due to convection, unmixed 316 stainless steel can be involved into the molten pool, solidifying rapidly into a peninsula near the CoCrFeMnNi side boundary, as illustrated in Fig. 10a C region. Conversely, near the CoCrFeMnNi HEA side, where $T_{L, bulk\ weld\ metal} \approx 1421°C > T \approx 1345°C$, the liquid weld metal solidifies first. It is then propelled by strong convection into the stagnant layer of liquid CoCrFeMnNi. Some liquid CoCrFeMnNi is pushed into the molten pool and has sufficient time to blend with the surrounding liquid weld metal due to overheating, resulting in the formation of a partially mixed zone, corresponding to region D of Fig. 10a. The remaining liquid of CoCrFeMnNi within the stagnant layer subsequently solidifies irregularly into separate CoCrFeMnNi zones, resembling beaches, as depicted in region E of Fig. 10a. Here, it is worth mentioning that future studies will employ high-energy synchrotron-based in-situ tensile testing to further investigate the phase transformation dynamics before and after fracture, especially considering the rich phases observed in the peninsula-shaped area.

In conclusion, the primary factors influencing macrosegregation in the dissimilar joints of CoCrFeMnNi HEA and 316 stainless steel are threefold: firstly, the inherent compositional differences between the two BMs; secondly, the disparities among the liquidus temperatures of the BMs and the bulk weld metal in the FZ; and thirdly, the strong convection and fluid flow effects during the non-equilibrium solidification process of welding. These factors work together to endow the joint with unique macro- and microstructural characteristics.

Conclusions

In this study, defect-free dissimilar welded joints between an as-rolled CoCrFeMnNi HEA and 316 stainless steel GTAW were obtained. The major conclusions of this study are outlined below:

1) Macroscopic segregation phenomena were observed in the FZ near the CoCrFeMnNi side, characterized by peninsular-shaped regions having compositions like that of the stainless steel BM. The occurrence of this macrosegregation phenomenon is linked to complex Marangoni flow effects, the lower liquidus temperature of bulk weld metal in the FZ compared to that of stainless steel BM, and the relatively narrow solidification temperature range.

2) Different degrees of softening behavior were observed in the HAZ near the CoCrFeMnNi side, attributed to recrystallization and grain growth effects induced by the weld thermal cycle.

3) Thermodynamic calculations tend to perform well in capturing the solidification phase structure formed during non-equilibrium rapid solidification processes. However, minor adjustments based on experimental results are still required for capturing the dynamics of phase transformations under actual welding conditions to be actually captured.

4) Fracture failure of the dissimilar welded joints occurred in the FZ, primarily attributed to the influence of large columnar grains, the presence of macrosegregation regions, and the formation of hard BCC and σ phases. The combined effect of these three factors led to the fracture failure of the welding joints.

Funding

References

[1] Cantor B, Chang ITH, Knight P, Vincent AJB (2004) Microstructural development in equiatomic multicomponent alloys. Mater Sci Eng A 375–377:213–218. https://doi.org/10.1016/j.msea.2003.10.257

[2] Lu K, Chauhan A, Litvinov D, Tirunilai AS, Freudenberger J, Kauffmann A, Heilmaier M, Aktaa J (2022) Micromechanical deformation behavior of CoCrFeMnNi high-entropy alloy. J Mater Sci Technol 100:237–245. https://doi.org/10.1016/j.jmst.2021.04.079

[3] Laplanche G, Kostka A, Horst OM, Eggeler G, George EP (2016) Microstructure evolution and critical stress for twinning in the CrMnFeCoNi high-entropy alloy. Acta Mater 118:152–163. https://doi.org/10.1016/j.actamat.2016.07.038

[4] Seifi M, Li D, Yong Z, Liaw PK, Lewandowski JJ (2015) Fracture Toughness and Fatigue Crack Growth Behavior of As-Cast High-Entropy Alloys. JOM 67:2288–2295. https://doi.org/10.1007/s11837-015-1563-9

[5] Xiong T, Yang W, Zheng S, Liu Z, Lu Y, Zhang R, Zhou Y, Shao X, Zhang B, Wang J, Yin F, Liaw PK, Ma X (2021) Faceted Kurdjumov-Sachs interface-induced slip continuity in the eutectic high-entropy alloy, AlCoCrFeNi2.1. J Mater Sci Technol 65:216–227. https://doi.org/10.1016/j.jmst.2020.04.073

[6] Zhou Y, Chen K, Ferreirós PA, Gao D, Song M, Shen Z, Que Z, Yu J, Zhang L, Zeng X (2025) Printed cellular structure enhancing re-passivation of stress corrosion cracking in high-temperature water. Corros Sci 244:112636. https://doi.org/10.1016/j.corsci.2024.112636

[7] Wang Z, Shen Z, Liu Y, Zhao Y, Zhu Q, Chen Y, Wang J, Li Y, Lozano-Perez S, Zeng X (2024) The effect of LPSO phase on the high-temperature oxidation of a stainless Mg-Y-Al alloy. J Magnes Alloy 12:4045–4052. https://doi.org/10.1016/j.jma.2024.07.009

[8] Ju J, Yu H, Zhao Y, Yang T, Xiao B, Peng P, Wang R, Wang H, Zeng X, Wang J, Shen Z (2024) Understanding the oxidation behaviors of a Ni-Co-based superalloy at elevated temperatures through multiscale characterization. Corros Sci 227:111800. https://doi.org/10.1016/j.corsci.2023.111800

[9] Chen Y, Ma S, Ju J, Chen K, Wang J, Shen Z, Zeng X (2025) Phase transformation-mediated high-temperature oxidation in an AlCrFeCoNi2.1 EHEA alloy at elevated temperature. Corros Sci 245:112674. https://doi.org/10.1016/j.corsci.2025.112674

[10] Nam H, Park C, Kim C, Kim H, Kang N (2018) Effect of post weld heat treatment on weldability of high entropy alloy welds. Sci Technol Weld Join 23:420–427. https://doi.org/10.1080/13621718.2017.1405564

[11] Nene SS, Liu K, Frank M, Mishra RS, Brennan RE, Cho KC, Li Z, Raabe D (2017) Enhanced strength and ductility in a friction stir processing engineered dual phase high entropy alloy. Sci Rep 7:16167. https://doi.org/10.1038/s41598-017-16509-9

[12] Lin J-Y, Lai Z-H, Otsuki T, Yen H-W, Nambu S (2021) Gradient microstructure and interfacial strength of CoCrFeMnNi high-entropy alloy in solid-state ultrasonic welding. Mater Sci Eng A 825:141885. https://doi.org/10.1016/j.msea.2021.141885

[13] Wu Z, David SA, Feng Z, Bei H (2016) Weldability of a high entropy CrMnFeCoNi alloy. Scr Mater 124:81–85. https://doi.org/10.1016/j.scriptamat.2016.06.046

[14] Jo M-G, Kim H-J, Kang M, Madakashira PP, Park ES, Suh J-Y, Kim D-I, Hong S-T, Han HN (2018) Microstructure and mechanical properties of friction stir welded and laser welded high entropy alloy CrMnFeCoNi. Met Mater Int 24:73–83. https://doi.org/10.1007/s12540-017-7248-x

[15] Hu Y, Niu Y, Zhao Y, Yang W, Ma X, Li J (2022) Friction stir welding of CoCrNi medium-entropy alloy: Recrystallization behaviour and strengthening mechanism. Mater Sci Eng A 848:143361. https://doi.org/10.1016/j.msea.2022.143361

[16] Kashaev N, Ventzke V, Stepanov N, Shaysultanov D, Sanin V, Zherebtsov S (2018) Laser beam welding of a

CoCrFeNiMn-type high entropy alloy produced by self-propagating high-temperature synthesis. Intermetallics 96:63–71. https://doi.org/10.1016/j.intermet.2018.02.014

[17] Lu Y, Zhang X, Wang H, Kan C, Zhang F, Dai P, Wang H (2022) Investigation of microstructure, texture, and mechanical properties of FeCoNiCrMn high entropy alloy during drive friction welding. Mater Charact 189:111959. https://doi.org/10.1016/j.matchar.2022.111959

[18] Wang G, Sheng G, Sun J, Wei Y, Gao X, Yu Z, Yuan X (2020) Mechanical properties and microstructure evolution of CrMnFeCoNi HEA/304 SS dissimilar brazing joints. J Alloys Compd 829:154520. https://doi.org/10.1016/j.jallcom.2020.154520

[19] Yao H, Chen K, Kondoh K, Dong X, Wang M, Hua X, Shan A (2022) Microstructure and mechanical properties of friction stir lap welds between FeCoCrNiMn high entropy alloy and 6061 Al alloy. Mater Des 224:111411. https://doi.org/10.1016/j.matdes.2022.111411

[20] Lin S (2019) Wu, Lin, Dissimilar Infrared Brazing of CoCrFe(Mn)Ni Equiatomic High Entropy Alloys and 316 Stainless Steel. Crystals 9:518. https://doi.org/10.3390/cryst9100518

[21] Sokkalingam R, Pravallika B, Sivaprasad K, Muthupandi V, Prashanth KG (2022) Dissimilar welding of high-entropy alloy to Inconel 718 superalloy for structural applications. J Mater Res 37:272–283. https://doi.org/10.1557/s43578-021-00352-w

[22] Zhang P, Qi Y, Cheng Q, Sun X (2024) Welding Dissimilar Alloys of CoCrFeMnNi High-Entropy Alloy and 304 Stainless Steel Using Gas Tungsten Arc Welding. J Mater Eng Perform 33:3273–3282. https://doi.org/10.1007/s11665-023-08229-1

[23] Xin J, Wang W, Yang X, Boubeche M, Wang S, Zhang H, Huang C, Li Y, Lyu B, Shen F, Sun W, Li L (2023) Dissimilar laser welding of CrMnFeCoNi high entropy alloy and 316LN stainless steel for cryogenic application. J Mater Sci Technol 163:158–167. https://doi.org/10.1016/j.jmst.2023.04.030

[24] Sokkalingam R, Mastanaiah P, Muthupandi V, Sivaprasad K, Prashanth KG (2020) Electron-beam welding of high-entropy alloy and stainless steel: microstructure and mechanical properties. Mater Manuf Process 35:1885–1894. https://doi.org/10.1080/10426914.2020.1802045

[25] Adomako NK, Kim JH (2021) Microstructure and mechanical properties of dissimilar laser lap joint between CoCrFeMnNi-high entropy alloy and duplex stainless steel. Mater Lett 288:129354. https://doi.org/10.1016/j.matlet.2021.129354

[26] Yao H, Wen H, Chen K, Jiang M, Reddy KM, Kondoh K, Wang M, Hua X, Shan A (2021) Interfacial phases formed in friction stir lap welding high entropy alloy to Al alloy. Scr Mater 201:113972. https://doi.org/10.1016/j.scriptamat.2021.113972

[27] Nam H, Park S, Chun E-J, Kim H, Na Y, Kang N (2020) Laser dissimilar weldability of cast and rolled CoCrFeMnNi high-entropy alloys for cryogenic applications. Sci Technol Weld Join 25:127–134. https://doi.org/10.1080/13621718.2019.1644471

[28] Oliveira JP, Shamsolhodaei A, Shen J, Lopes JG, Gonçalves RM, de Brito Ferraz M, Piçarra L, Zeng Z, Schell N, Zhou N, Seop Kim H (2022) Improving the ductility in laser welded joints of CoCrFeMnNi high entropy alloy to 316 stainless steel. Mater Des 219:110717. https://doi.org/10.1016/j.matdes.2022.110717

[29] Do H, Asadi S, Park N (2022) Microstructural and mechanical properties of dissimilar friction stir welded CoCrFeMnNi high entropy alloy to STS304 stainless steel. Mater Sci Eng A 840:142979. https://doi.org/10.1016/j.msea.2022.142979

[30] Adomako NK, Shin G, Park N, Park K, Kim JH (2021) Laser dissimilar welding of CoCrFeMnNi-high entropy alloy and duplex stainless steel. J Mater Sci Technol 85:95–105. https://doi.org/10.1016/j.jmst.2021.02.003

[31] Sokkalingam R, Muthupandi V, Sivaprasad K, Prashanth KG (2019) Dissimilar welding of Al 0.1 CoCrFeNi high-entropy alloy and AISI304 stainless steel. J Mater Res 34:2683–2694. https://doi.org/10.1557/jmr.2019.186

[32] Oliveira JP, Shen J, Zeng Z, Park JM, Choi YT, Schell N, Maawad E, Zhou N, Kim HS (2022) Dissimilar laser welding of a CoCrFeMnNi high entropy alloy to 316 stainless steel. Scr Mater 206:114219. https://doi.org/10.1016/j.scriptamat.2021.114219

[33] Wang L, Ma X, Mi G, Su L, Zhu Z (2023) Microstructural Inhomogeneity in the Fusion Zone of Laser Welds. Materials (Basel) 16:7053. https://doi.org/10.3390/ma16217053

[34] Oliveira JP, Zeng Z, Andrei C, Braz Fernandes FM, Miranda RM, Ramirez AJ, Omori T, Zhou N (2017) Dissimilar laser welding of superelastic NiTi and CuAlMn shape memory alloys. Mater Des 128:166–175. https://doi.org/10.1016/j.matdes.2017.05.011

[35] Soysal T, Kou S, Tat D, Pasang T (2016) Macrosegregation in dissimilar-metal fusion welding. Acta Mater 110:149–160. https://doi.org/10.1016/j.actamat.2016.03.004

[36] Shen J, Kim RE, He J, Lopes JG, Yang J, Zeng Z, Schell N, Kim HS, Oliveira JP (2025) Gas tungsten arc welding of CoCrFeMnNi high entropy alloy to 316 stainless steel.

Mater Sci Eng A 922:147664. https://doi.org/10.1016/j.msea.2024.147664

[37] Shen J, Gonçalves R, Choi YT, Lopes JG, Yang J, Schell N, Kim HS, Oliveira JP (2023) Microstructure and mechanical properties of gas metal arc welded CoCrFeMnNi joints using a 308 stainless steel filler metal. Scr Mater 222:115053. https://doi.org/10.1016/j.scriptamat.2022.115053

[38] David SA, Babu SS, Vitek JM (2003) Welding: Solidification and microstructure. JOM 55:14–20. https://doi.org/10.1007/s11837-003-0134-7

[39] Hsieh C-C, Wu W (2012) Overview of Intermetallic Sigma () Phase Precipitation in Stainless Steels. ISRN Metall 2012:1–16. https://doi.org/10.5402/2012/732471

[40] Erneman J, Schwind M, Liu P, Nilsson J-O, Andrén H-O, Ågren J (2004) Precipitation reactions caused by nitrogen uptake during service at high temperatures of a niobium stabilised austenitic stainless steel. Acta Mater 52:4337–4350. https://doi.org/10.1016/j.actamat.2004.06.001

[41] Erneman J, Schwind M, Andren H, Nilsson J, Wilson A, Agren J (2005) The evolution of primary and secondary niobium carbonitrides in AISI 347 stainless steel during manufacturing and long-term ageing. Acta Mater 54:67–76. https://doi.org/10.1016/j.actamat.2005.08.028

[42] Yoon J-H, Yoon E-P, Lee B-S (2007) Correlation of chemistry, microstructure and ductile fracture behaviours of niobium-stabilized austenitic stainless steel at elevated temperature. Scr Mater 57:25–28. https://doi.org/10.1016/j.scriptamat.2007.03.025

[43] Barcik J (1983) The kinetics of σ-phase precipitation in AISI310 and AISI316 steels. Metall Trans A 14:635–641. https://doi.org/10.1007/BF02643779

[44] Slattery GF, Keown SR, Lambert ME (1983) Influence of δ-ferrite content on transformation to intermetallic phases in heat-treated, type 316 austenitic stainless steel weld metal. Met Technol 10:373–385. https://doi.org/10.1179/030716983803291208

[45] Singhal L, Martin J (1968) The formation of ferrite and sigma-phase in some austenitic stainless steels. Acta Metall 16:1441–1451. https://doi.org/10.1016/0001-6160(68)90039-4

[46] Kim Y-K, Joo Y-A, Kim HS, Lee K-A (2018) High temperature oxidation behavior of Cr-Mn-Fe-Co-Ni high entropy alloy. Intermetallics 98:45–53. https://doi.org/10.1016/j.intermet.2018.04.006

[47] Shen J, Gonçalves R, Choi YT, Lopes JG, Yang J, Schell N, Kim HS, Oliveira JP (2022) Microstructure and mechanical properties of gas metal arc welded CoCrFeMnNi joints using a 410 stainless steel filler metal. Mater Sci Eng A 857:144025. https://doi.org/10.1016/j.msea.2022.144025

[48] Perron A, Toffolon-Masclet C, Ledoux X, Buy F, Guilbert T, Urvoy S, Bosonnet S, Marini B, Cortial F, Texier G, Harder C, Vignal V, Petit P, Farré J, Suzon E (2014) Understanding sigma-phase precipitation in a stabilized austenitic stainless steel (316Nb) through complementary CALPHAD-based and experimental investigations. Acta Mater 79:16–29. https://doi.org/10.1016/j.actamat.2014.06.066

[49] Yadollahi A, Shamsaei N, Thompson SM, Seely DW (2015) Effects of process time interval and heat treatment on the mechanical and microstructural properties of direct laser deposited 316L stainless steel. Mater Sci Eng A 644:171–183. https://doi.org/10.1016/j.msea.2015.07.056

[50] Järvinen J-P, Matilainen V, Li X, Piili H, Salminen A, Mäkelä I, Nyrhilä O (2014) Characterization of Effect of Support Structures in Laser Additive Manufacturing of Stainless Steel. Phys Procedia 56:72–81. https://doi.org/10.1016/j.phpro.2014.08.099

[51] Zhao J, Zhang B, Li X, Li R (2015) Effects of metal-vapor jet force on the physical behavior of melting wire transfer in electron beam additive manufacturing. J Mater Process Technol 220:243–250. https://doi.org/10.1016/j.jmatprotec.2015.01.024

[52] Skiba T, Baufeld B, van der Biest O (2009) Microstructure and Mechanical Properties of Stainless Steel Component Manufactured by Shaped Metal Deposition. ISIJ Int 49:1588–1591. https://doi.org/10.2355/isijinternational.49.1588

[53] Conejero O, Palacios M, Rivera S (2009) Premature corrosion failure of a 316L stainless steel plate due to the presence of sigma phase. Eng Fail Anal 16:699–704. https://doi.org/10.1016/j.engfailanal.2008.06.022

[54] Qin G, Chen R, Zheng H, Fang H, Wang L, Su Y, Guo J, Fu H (2019) Strengthening FCC-CoCrFeMnNi high entropy alloys by Mo addition. J Mater Sci Technol 35:578–583. https://doi.org/10.1016/j.jmst.2018.10.009

[55] Park SHC, Sato YS, Kokawa H, Okamoto K, Hirano S, Inagaki M (2003) Rapid formation of the sigma phase in 304 stainless steel during friction stir welding. Scr Mater 49:1175–1180. https://doi.org/10.1016/j.scriptamat.2003.08.022

[56] Guilherme LH, Benedetti AV, Fugivara CS, Magnabosco R, Oliveira MF (2020) Effect of MAG welding transfer mode on sigma phase precipitation and corrosion performance of 316L stainless steel multi-pass welds. J Mater Res Technol 9:10537–10549. https://doi.org/10.1016/j.jmrt.2020.07.039

[57] Shen J, Lopes JG, Zeng Z, Choi YT, Maawad E, Schell N, Kim HS, Mishra RS, Oliveira JP (2023) Deformation behavior and strengthening effects of an eutectic AlCoCrFeNi2.1 high entropy alloy probed by in-situ synchrotron X-ray diffraction and post-mortem EBSD. Mater Sci Eng A 872:144946. https://doi.org/10.1016/j.msea.2023.144946

[58] Wang R (2021) Precipitation of sigma phase in duplex stainless steel and recent development on its detection by

electrochemical potentiokinetic reactivation: A review. Corros Commun 2:41–54. https://doi.org/10.1016/j.corcom.2021.08.001

[59] Dong Q, Chen X, Nagaumi H, Wang X, Zhang B (2022) Formation mechanism of macrosegregation in dissimilar-filler welding of aluminum alloys. J Mater Res Technol 20:26–34. https://doi.org/10.1016/j.jmrt.2022.07.074

[60] Sun Q, Chen J, Wang X, Gu F, Tan C, Shamsolhodaei A, Sun L, Zhou YN (2021) Study on weld formation and segregation mechanism for dissimilar pulse laser welding of NiTi and Cu wires. Opt Laser Technol 140:107071. https://doi.org/10.1016/j.optlastec.2021.107071